Sustainable Cities and Society 125 (2025) 106350

Contents lists available at ScienceDirect

Sustainable Cities and Society

journal homepage: www.elsevier.com/locate/scs

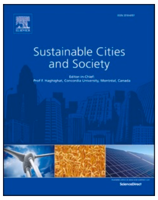

Precise mitigation strategies for urban heat island effect in Hong Kong's new towns using automated machine learning

Yiyan Li [a,b], Hongsheng Zhang [a,b,*], Yinyi Lin [a,b,*], Jing Ling [c], Huiyuan Xue [d], Peizhuo Guo [d]

[a] Department of Geography, The University of Hong Kong, Hong Kong, China
[b] The University of Hong Kong Shenzhen Institute of Research and Innovation, Shenzhen, China
[c] School of Information Engineering, Guangdong University of Technology, Guangzhou, China
[d] Department of Urban Planning and Design, The University of Hong Kong, Hong Kong, China

ARTICLE INFO

Keywords:
Urban heat island
Built environment
Automated machine learning
Shapley additive explanations (SHAP)
New town

ABSTRACT

New town developments aim to enhance the spatial layout and quality of living environments in metropolitan areas. These areas are vulnerable to the urban heat island (UHI) effect owing to high-density development and poor long-term planning. However, few studies have investigated the spatial distribution of the influence of built environments on UHI, limiting the ability of urban planners to develop targeted mitigation strategies. To address this gap, we analyzed the complex spatial relationship between land surface temperature (LST), an important indicator of UHI, and the built environment in all new towns in Hong Kong. We employed remote sensing images, street view images, geographical information science (GIS) data, and land-use data with automated machine learning to model the LST-built environmental relationship at various spatial scales, using Shapley Additive Explanations (SHAP) to interpret the model to show the spatial distribution of the influence of the built environment on UHI. Our best model was the Extreme Gradient Boosting Machine model with a 210-m grid R-squared value of 0.79. We found that 1) the land-use feature class had the most significant influence on LST, and 2) there was spatial heterogeneity among the major contributors to UHI. The refined UHI attribution analysis method proposed in this study enables precise modeling for smart and sustainable city planning. (211 words)

1. Introduction

Rapid urbanization continues to reshape the global landscape. By 2050, the urban population is projected to account for 68 % of the global population (United Nations, Department of Economic, Social Affairs, & Population Division, 2018). This intense urbanization has brought various environmental challenges (Ling et al., 2024), among which the urban heat island (UHI) effect has emerged as a critical issue affecting urban sustainability and human well-being. The UHI effect describes the phenomenon in which urban areas experience higher temperatures than the surrounding rural areas (Huang et al., 2019). UHI significantly affects temperature-related health (Islam et al., 2024). This increases the frequency of heat anomalies and the risk of heat-related mortality in urban areas. The adverse effects of UHI are particularly pronounced for vulnerable populations (Heaviside et al., 2017), including the elderly and children (Cornu et al., 2024). Furthermore, this leads to higher energy consumption by increasing the building demand for temperature adjustment (Guattari et al., 2018). Depending on the building type, UHI can increase cooling-related energy consumption by 10–70 % (Litardo et al., 2020).

There are two main data sources for measuring UHI: air temperature data recorded by weather stations and surface temperatures calculated based on remote sensing images (Zhang et al., 2022). The weather station data are more accurate. However, because of the distance between stations, it is difficult to demonstrate high-spatial-resolution temperature transformations (Wang & al., 2023). Outliers are more likely to occur because a limited station count is sensitive to environmental influences (Yang et al., 2023). Land-surface temperature (LST) calculations from remote sensing data are widely used in UHI correlation research (Wei et al., 2023; Bagyaraj et al., 2023; Li et al., 2018). The index has been shown to be highly correlated with weather station records and provide continuous changes in UHI (Li et al., 2018; do Nascimento et al., 2022).

Understanding how urban-built environmental features influence

---

* Corresponding author at: The University of Hong Kong, Room 1007, 10/F, The Jockey Club Tower, Hong Kong, , China.
E-mail addresses: u3603818@connect.hku.hk (Y. Li), zhanghs@hku.hk (H. Zhang), yinyilin@link.cuhk.edu.hk (Y. Lin), lingjing@gdut.edu.cn (J. Ling), xuehy@hku.hk (H. Xue), takukpt@hku.hk (P. Guo).

https://doi.org/10.1016/j.scs.2025.106350
Received 15 August 2024; Received in revised form 30 March 2025; Accepted 31 March 2025

UHI can help guide urban cooling strategies. The built environment is a key factor influencing the UHI effect. Based on multi-source spatial data, researchers have examined various built environmental features that affect UHI. These features include: (1) land cover and land-use features, such as the area proportion of different land-use types (Aydin et al., 2024); (2) building and infrastructure features, such as mean building density, building height and road density (Lin et al., 2023; Zhang et al., 2024; Liu et al., 2023); (3) three-dimensional morphological features, such as the sky view factor (SVF) and FAI (Wei et al., 2023; Chen et al., 2025; Yang et al., 2019); (4) street-level features, such as the green view index (GVI) and building view index (BVI) (Wei et al., 2023); (5) socioeconomic factors, such as population and points of interest density (Singh et al., 2024; Jiang et al., 2024); and (6) remote sensing indices, such as normalized difference vegetation index (NDVI) and normalized difference vegetation index (NDBI) (Hu et al., 2020; Gao et al., 2022).

To analyze these built environmental features and their impacts on UHI, researchers have primarily employed two approaches: physical simulation and mathematical modeling. Physical simulation methods provide a detailed analysis of thermal conditions in built environments. ENVI-met, a prominent simulation tool, employs computational fluid dynamics to model urban thermal environments based on comprehensive spatial data including building morphology, street patterns, vegetation distribution, and surface materials (Banerjee et al., 2024). Recent studies have demonstrated the analytical capabilities of this method. Banerjee et al. (2024) used ENVI-met to evaluate the thermal impacts of various building regulations across urban blocks. Similarly, Darbani et al. (2023) examined the thermal conditions in Mashhad, Iran, and investigated the relationships between SVF, building materials, and thermal patterns. Despite their analytical strengths, physical simulations have significant operational constraints. The method requires substantial computational resources (Balany et al., 2020). Aleksandrowicz et al. (2023) reported that simulations require several hours of processing time even for a limited spatial extent. These computational demands restrict analyses to small urban areas (Darbani et al., 2023; Li et al., 2023; Sinsel et al., 2022; Cui et al., 2024). Thus, although physical simulations offer precise microscale analysis, application at broader urban scales remains challenging.

Mathematical modeling approaches have evolved significantly in recent years. Initially, researchers used linear regression to quantify the relationships between built environmental features and UHI (Shi et al., 2019; Chiang et al., 2023). However, owing to restrictions on the linear independence of variables in linear regression, relevant studies can usually only select four to five variables (Zhang et al., 2024). Furthermore, there is a potential nonlinear relationship between thermal and built environments (Chen et al., 2025; Lin, Wei, & Guan, 2024). Linear regression models have difficulty capturing this relationship. Recent studies have shifted toward machine learning methods to address these limitations (Wang et al., 2023; Lin et al., 2023; Lin, et al., 2024; Acosta et al., 2023). These models excel at processing large datasets and identifying non-linear patterns (Wei et al., 2023). However, machine learning models lack interpretability (Lin et al., 2023) and typically produce global simulations (Werner et al., 2020), failing to reveal spatial variations in UHI relationships. Researchers have explored alternative methods to address the spatial heterogeneity of the influence of built environments on UHI. Geographically weighted regression (GWR) enables the analysis of spatial variations in built environment-UHI relationships (Gao et al., 2022; Zhou et al., 2024; Zhang et al., 2022). Although GWR effectively captures spatial heterogeneity, it retains the limitations of linear models in expressing non-linear relationships. In response, researchers have developed geographically weighted machine learning algorithms that can generate specific models for subregions and examine the distribution of feature importance (Zhang et al., 2024). For example, Zhang et al. (Zhang et al., 2024) employed geographical weighted random forest (GWRF) to analyze spatial variations in green space impacts on the thermal environment of Beijing. However, these methods only reveal the spatial patterns of feature importance without demonstrating the specific contributions of built environmental features to UHI.

In summary, current studies face challenges in quantifying the spatial distribution of the impact of built environments on UHI. The computational requirements of physical simulations limit their application at larger urban scales. Different mathematical modeling methods have their own limitations: linear regression models and GWR struggle to handle multivariate and nonlinear relationships; machine learning methods lack interpretability and can only provide global results; and geographically weighted machine learning methods, such as GWRF, only reveal spatial patterns of feature importance without quantifying the specific impacts of built environmental characteristics at different locations. This makes it difficult for decision makers to accurately grasp the actual contribution of various built environmental factors to the UHI in different regions, affecting the accuracy and efficiency of cooling strategies. Therefore, accurate quantification of the specific impact of each built environment feature on UHI at different locations while maintaining the nonlinear capturing ability of the model remains an urgent problem in this field. Machine learning interpretability techniques, particularly Shapley Additive Explanations (SHAP), have provided opportunities to address the "black box" problem in machine learning models (Wang et al., 2024). In UHI research, studies have primarily used SHAP to explain global feature importance and the nonlinear influence of built environmental features on UHI (Chen et al., 2025; Wang et al., 2024; Kim & Kim, 2022). However, in addition to providing global explanations for machine-learning models, applications of SHAP in other areas, such as traffic accident analysis and landslide assessment, have demonstrated its potential for quantifying the effects of spatial variables (Jiang et al., 2024; Xue et al., 2024). This indicates that it has broad application prospects for quantifying the local effects of built environmental features on UHI. Therefore, this study proposed a "machine learning + SHAP value spatial analysis" method, taking the new towns of Hong Kong as an example to explore the spatial distribution of the influence of built environment characteristics on UHI. First, we collected and integrated multisource data to quantify the built environment. Subsequently, we used automated machine learning and Bayesian optimization techniques to generate optimal machine learning models from multiscale grids. Finally, we used the SHAP methodology to explain the optimal machine learning model and discuss how the characteristics of the built environment affect the UHI in each grid.

2. Study area

The development of new towns aims to improve the spatial layout and quality of living environments. High-density compact development and insufficient long-term land-use planning are more susceptible to UHI effects (Yin et al., 2018). Hong Kong serves as a representative example of a rapidly developing and high-density city (Bagyaraj et al., 2023), making it highly relevant for studying the impact of building environments on UHI in new towns. Therefore, we selected new towns in Hong Kong as our study area (Fig. 1). The Hong Kong government divided the nine new towns into three generations: the first generation of new towns, Tsuen Wan, Sha Tin, and Tuen Mun, began construction in the early 1970s; the second generation of new towns, Tai Po, Fanling/Sheung Shui, and Yuen Long, began construction in the late 1970s; and the third generation of new towns, Tseung Kwan O, Tin Shui Wai, and Tung Chung, began construction between 1980 and 1990 (Civil Engineering and Development Department, 2016), with a total area of 1133.72 km^2, accounting for 53.49 % of the built-up area in Hong Kong. The total population of these new towns was 32,698,000, accounting for 43.58 % of the' total population in Hong Kong.

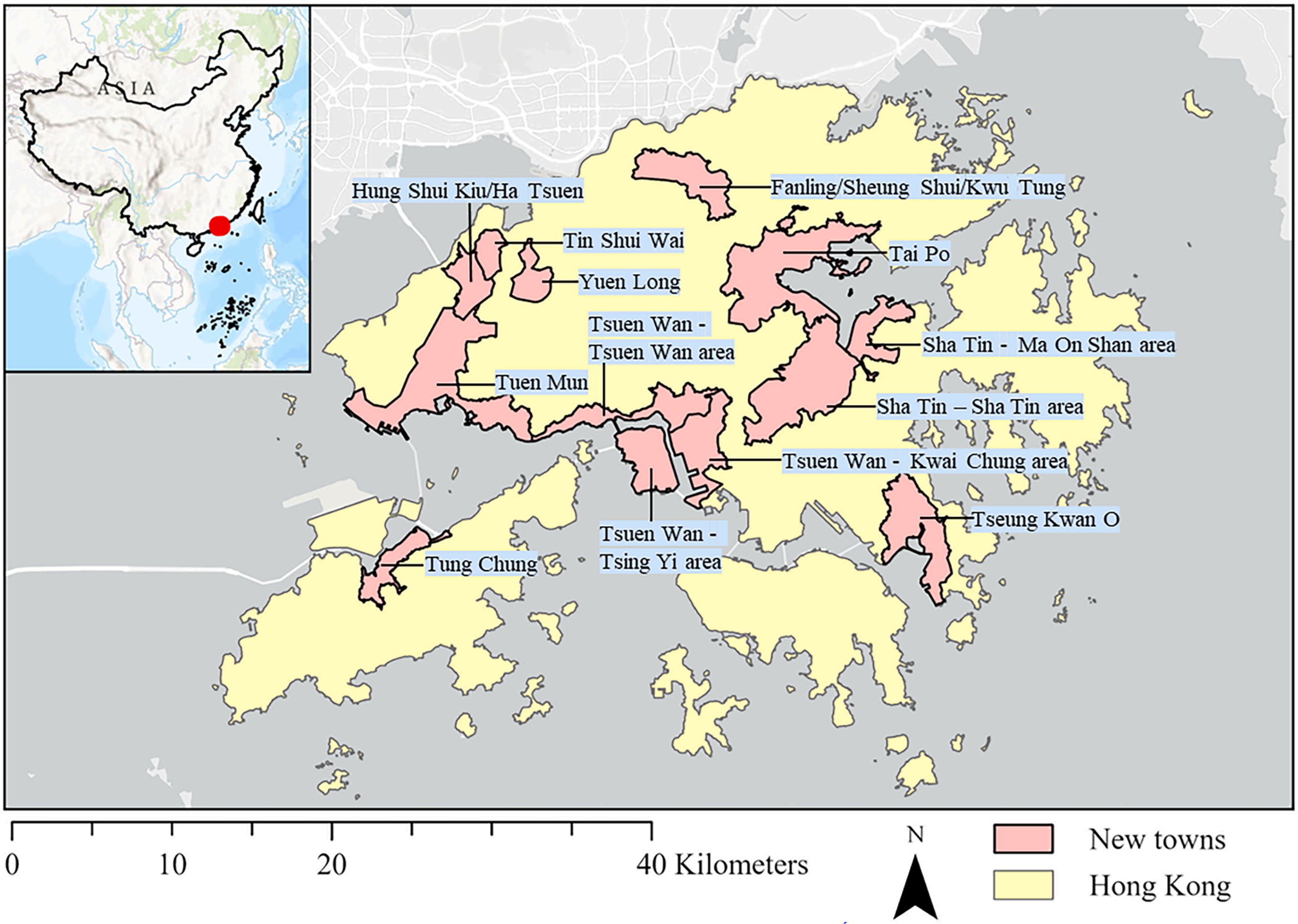

Fig. 1. Geographical location of new towns in Hong Kong.

3. Data and methodology

3.1. Data

In this study, the LST of the new towns in Hong Kong was extracted as the dependent variable, based on remote sensing images. In addition, we collected multisource urban geospatial datasets to quantify built environmental features from three dimensions: land use, building facilities, and pedestrian perspectives.

3.2. Research framework

The experimental procedure is illustrated in Fig. 2. First, we extracted built environmental features from street view images, urban facility information data, and land-use layers, each from a pedestrian, facilities, and land-use perspective. Subsequently, both the LST and built environmental features within each grid were statistically analyzed. Automatic machine learning and Bayesian optimization were used in the modeling to generate the optimal model. Finally, an artificial intelligence technique, SHAP, was used to interpret the optimal model and explore the spatial distribution of the influence of the built environment on UHI. Currently, there is no unified standard for the spatial scale of units used in modeling surface temperature predictions (Wei et al., 2023). Moreover, the spatial scale can influence the performance of surface temperature fitting models (Wei et al., 2023; Yang et al., 2019). Therefore, we investigated the influence of the building environment on surface temperature at different grid sizes with a spatial resolution of 30 m. We considered grid sizes of 60, 90, 120, 150, 180, 210, and 240 m to explore the effects. To ensure an adequate number of samples for subsequent modeling, larger grid sizes were not considered.

3.2.1. Built environmental features

Based on a review of the existing literature, we collected 50 potential building environmental features that could influence the UHI effect. These features were systematically categorized into three levels to reflect the different scales of urban planning and design interventions. At the macro level, land-use features represent the fundamental urban planning elements that shape the overall city structure. At the regional level, facility-related features capture the medium-scale building environmental elements that define community characteristics. At the micro level, streetscape information includes fine-grained landscape features that directly influence the human experience and local thermal environments. This multiscalar classification framework systematically examines how building environmental features at different planning levels impact urban heat patterns.Table 2 presents a detailed compilation of these environmental features.

3.2.2. Data preprocessing

3.2.2.1. Extraction of land surface temperature. LST is widely recognized as an important indicator of UHI (Huang et al., 2019; Wei et al., 2023; Bagyaraj et al., 2023), and Hong Kong has the highest temperature in summer (June to September). This led to spikes in electricity consumption in certain sectors. At the same time, human health is seriously threatened by high temperatures. In addition, sunny weather results in stronger UHI. This has exacerbated the adverse impact of high summer temperatures on the energy consumption and resident health in Hong Kong. From the perspective of urban planning, planners and architects

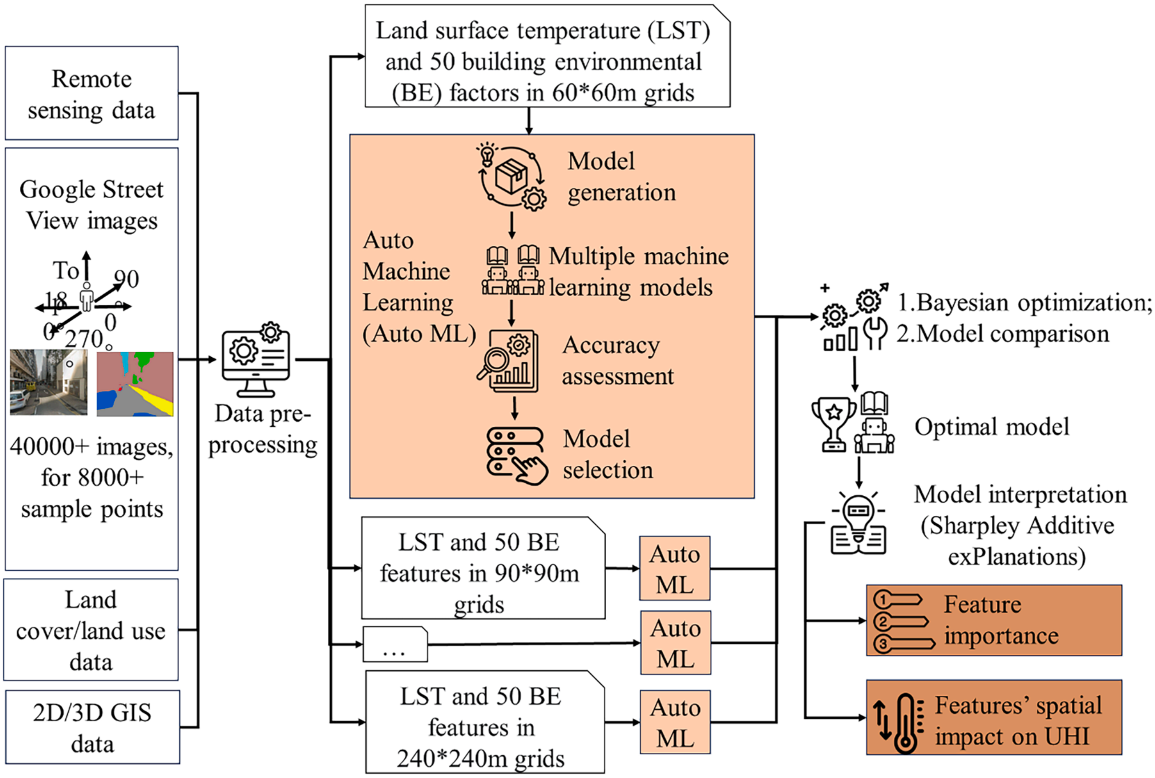

Fig. 2. Research workflow.

Table 1
summarizes the data used in this study.

Table 1. Summary of Data Sources for Quantifying Building Environment

Dimension	Name	Source	Format
Source of LST data			
–	Landsat 8–9 OLI and TIRS Collection 2 Level-1	EarthExplorer (usgs.gov)	Geotiff
Data sources of built environment characteristics			
Land use	LUMHK_RasterGrid_2022	Planning Department - Land Utilization in Hong Kong (pland.gov.hk)	Geotiff
Facilities	Road Network Data of Hong Kong	https://opendata.esrichina.hk/datasets	Shapefile
	3D Pedestrian Network in Hong Kong	https://opendata.esrichina.hk/datasets	Shapefile
	Building footprint	https://opendata.esrichina.hk/datasets/building	Shapefile
	Bus Stop Locations in Hong Kong	https://opendata.esrichina.hk/maps/esrihk::bus-stop-locations-in-hong-kong	Shapefile
	Shuttle Radar Topography Mission (SRTM)	EarthExplorer (usgs.gov)	Geotiff
Street view images	Google street view (GSV) images	Downloaded through Google API	jpg

should prioritize summer conditions as a key design scheme (Giridharan et al., 2007). Therefore, we searched for Landsat8 data with less than 20 % cloud cover from June to September 2022. Only one image from Hong Kong met these criteria. Based on this image, we used the mono-window method for LST calculations (Bagyaraj et al., 2023), as follows:

$$TOA = 0.0003342 \times \text{Band } 10 + 0.1 \tag{1}$$

$$BT = K_2/(\ln(K_1 / TOA) + 1) - 273.15 \tag{2}$$

$$NDVI = (Band5 - Band4)/(and5 + Band4) \tag{3}$$

$$Pv = (NDVI - NDVI_{min})/(NDVI_{max} - NDVI_{min}) \tag{4}$$

$$\varepsilon = 0.04 \times \text{Pv} + 0.986 \tag{5}$$

$$LST = BT/(1 + (0.00115 \times BT / 14388) \times \ln(\varepsilon)) \tag{6}$$

where TOA represents Top of Atmospheric, Band 10 is the 10th band of Landsat 8, *BT* represents Brightness Temperature, K_1 is the band-specific thermal conversion constant of band 10, K_2 is the band-specific thermal conversion constant of band 10, *NDVI* is the Normalized Difference Vegetation Index, *Pv* represents the proportion of vegetation, and ε represents the emissivity coefficient (Bagyaraj et al., 2023). We used the raster calculator function in ArcGIS Pro to complete the LST calculations.

3.2.2.2. Data sources and extraction of land-use features. Land-use data provide official and authoritative urban planning information and are considered a driving factor that determines surface radiation and surface energy conversion, directly influencing the surface temperature (Shi et al., 2019; Yin et al., 2018). To generate this dataset, land utilization in Hong Kong employed various geospatial technologies, including the latest satellite imagery, internal survey data, and other relevant information from government departments (Planning Department, 2023). The dataset had a spatial resolution of 10 m and included 30 land-use categories. Although there is no uniform land-use classification standard in the study of UHI (Wei et al., 2023; Hu et al., 2020), researchers have used local governmental land classification reports as a standard for land classification. Therefore, we followed the land-use classification system of the Hong Kong government and calculated the percentage of each land-use category within the study area as a land-use feature. We calculated the proportion of different land-use types in each grid using the ArcGIS Pro platform.

Table 2
Introduction of the built environmental features.

Feature class	Feature name	Description	References
Landuse feature class	Grassland	the proportion of grassland to the grid	(Aydin et al., 2024)
	Woodland	the proportion of woodland to the grid	
	Shrubland	the proportion of shrubland to the grid	
	Rural_Settlement	the proportion of rural settlement land to the grid	
	VL_CiP	the proportion of Vacant land (construction in progress) to the grid	
	Agricultural_Land	the proportion of agricultural land to the grid	
	Utilities	the proportion of utilities to the grid	
	R_and_TF	the proportion of roads and transport facilities to the grid	
	WH_and_OS	the proportion of warehouse and open storage to the grid	
	CF_Facilities	the proportion of cemeteries funeral facilities to the grid	
	Industrial_Land	the proportion of industrial land to the grid	
	GI_and_CF	the proportion of government, institutional and community facilities to the grid	
	Streams_Nullahs	the proportion of streams and nullahs to the grid	
	Fish_Ponds	the proportion of fish ponds land use to the grid	
	OS_and_RL	the proportion of open space and recreational land to the grid	
	Private_Residential	the proportion of private residential land to the grid	
	CB_and_O	the proportion of commercial, business and office land to the grid	
	Railways	the proportion of railways land to the grid	
	Public_Residential	the proportion of public residential to the grid	
	Rocky_Shore	the proportion of rocky shore to the grid	
	MangroveSwamp	the proportion of mangrove swamp land to the grid	
	Reservoirs	the proportion of land to the grid	
	IE_andTP	the proportion of reservoirs to the grid	
	Badland	the proportion of badland to the grid	
	Port_Facilities	the proportion of port facilities land to the grid	
	Others	the proportion of other kind land use to the grid	
Facility feature class	trans_len	The total length of traffic road within a grid	(Lin et al., 2023)
	trans_count	The count of traffic road in a grid	This study
	ped_len	The total length of sidewalks within a grid	This study
	ped_count	The count of sidewalks in a grid	This study
	bus_count	The count of bus stations in a grid	This study
	sum_volume	The total building volume in a grid	(Chen et al., 2025)
	sum_surface_a	The total building surface area in a grid	This study
	sum_height	The total building height in a grid	This study
	mean_height	The mean building height in a grid	(Singh, et.al, 2024)
	bd_count	The number of the building in a grid	(Gao, et al., 2022)
	footprint_a	The floor area of the building	(Singh, et al., 2024)
	FAI	Frontal area index, the ratio that measures the total area of each building facade projected onto a plane perpendicular to the prevailing wind direction, divided by the area of the grid. It provides information about the wind environment within the grid	(Yang et al., 2019)
	DEM_std	The standard deviation of the digital terrain height in the grid, which is used to reflect the relief of the terrain	This study
	SSC	Sun shadow coverage, the proportion of the shadow coverage area of the building to the grid area	(Chen et al. 2023)
	SSF	Sun shadow frequency, refers to the rate at which shadows are cast by the sun over a given period of time	(Park, Z, Guldmann & Wentz, 2023)
GSV feature class	mean_p_tree	The average proportion of trees in the horizontal field of view across all street-level sampling points within the grid	(Wei et al., 2023)
	mean_p_grass	The average proportion of grass in the horizontal field of view across all street-level sampling points within the grid	
	mean_p_water	The average proportion of grass in the horizontal field of view across all street-level sampling points within the grid	
	mean_p_building	The average proportion of buildings in the horizontal field of view across all street-level sampling points within the grid	
	mean_p_road	The average proportion of roads in the horizontal field of view across all street-level sampling points within the grid	
	mean_p_sidewalk	The average proportion of sidewalks in the horizontal field of view across all street-level sampling points within the grid	
	mean_svf	The average sky view factor of all Street View sampling points in the grid	
	mean_tvf	The average tree view factor of all Street View sampling points in the grid	
	mean_bvf	The average building view factor of all Street View sampling points in the grid	

3.2.2.3. Data sources and facility feature extraction. The data used to extract facility features included road networks, building footprints, bus stops, and digital elevation data, primarily sourced from the ESRI Hong Kong platform. Using these datasets, we calculated the number of roads, road lengths, number of sidewalks, sidewalk lengths, number of bus stops, building density, building footprint area, building volume, building surface area, and average building height in the study area. Additionally, we simulated building shadow frequency and coverage using the "Sun Shadow Frequency" tool in ArcGIS Pro, as shadows are key to influencing UHI (Park et al., 2021). In the "Sun Shadow Frequency" function, we made the following settings: (1) set the Hong Kong three-dimensional (3D) building model as the input feature; (2) set the Hong Kong shuttle radar topography mission (SRTM) data as the ground surface; and (3) set the acquisition time (local time: 2022–09–03 10:52:22) of the remote sensing image as the end time to simulate sun shadow coverage. In addition to shadow coverage, the frequency of shadow coverage was considered. As the effect of the shadow is cumulative, its cooling effect continues and intensifies the longer it remains at the same position (Park et al., 2023). While keeping the sun shadow coverage settings unchanged, we set 2022–09–03 10:52:22 as the start time and counted the cumulative effect of the shadow coverage at a frequency of 30 min. The number of times the shadows were covered was counted as the sun-shadow frequency. Moreover, the frontal area index (FAI), a coefficient representing the area of urban buildings blocking wind, is highly correlated with UHI (Yang et al., 2019). The formula for calculating FAI is as follows:

$$\lambda_f(\theta) = A_{proj}/A_t \tag{7}$$

where $\lambda_f(\theta)$ represents the FAI in the southeastern wind direction, A_{proj} represents the total area of each building facet projected onto the plane normal to the incoming wind direction, and A_t represents the grid area. We calculated the FAI using the 3D information of the buildings in Python.

SRTM data were provided by NASA. This dataset consists of global 30-m resolution digital elevation model (DEM) data obtained through laser radar observations. Terrain undulations can influence the layout and planning of infrastructure (e.g., roads and buildings) (Yang et al., 2022). Therefore, we calculated the standard deviation of the DEM values within each grid to quantify the terrain variability.

3.2.2.4. Data sources and extraction of the google street view features. Street-view information is highly correlated with UHI effects and LST (Chiang et al., 2023; Zhou et al., 2022). Compared to land-use data, it offers more vertical structural information and enhances surface temperature models (Wang et al., 2021). We sampled evenly at 50 m intervals across the road network, resulting in 25,438 sampling points. For each coordinate, we downloaded images at horizontal angles of 0°, 30°, 60°, and 90° relative to the driving direction as well as images with a 90° elevation angle.

We used the Deeplab_resnet101_ade model (Zhang et al., 2022) for the semantic segmentation of the collected Google Street View (GSV) images. The model was trained on the ADE20K dataset and recognized 35 staff classes (such as walls, sky, and roads) (Zhou et al., 2017) with a pixel accuracy of 81.1 % (Zhang et al., 2022). We calculated nine GSV-built environmental features (proportion of trees, grass, water, buildings, roads, and sidewalks in the horizontal view and proportion of trees, sky, and buildings in the upward view). Eq. (8) uses GVI as an example to illustrate the process of calculating GSV-built environmental features (Lu, 2018):

$$GVI = \sum_{i=1}^{4} Greenery\ pixcels_i \Bigg/ \sum_{i=1}^{4} Total\ pixcels_i \tag{8}$$

Because we took four street views at 90° in the horizontal direction for each observation point, the horizontal street view information for the observation point was needed to sum the number of street view objects in the four directions. The methodologies for calculating the horizontal and up view street-view information are largely similar. However, for up-view street-view information, we captured only one image per observation point. Consequently, the analysis of up-view street-view information involves merely quantifying the proportion of various street-view objects within a single image.

3.2.3. *Modeling and validation*

To screen for the most suitable grid scale and model, we divided the samples under each grid scale into 70 % and 30 % groups. Seventy percent of the samples were used for training, and the remaining 30 % **of** the samples were used for testing. Based on the training samples, we utilized automatic machine learning to build multiple machine learning models for each grid scale. The five-fold cross-validation method was used to evaluate the model performance. Subsequently, for each grid scale, we selected the best-performing models and adjusted their hyperparameters using Bayesian optimization. The five-fold cross-validation method was then used to test the accuracy of the models with different combinations of hyperparameters. The model with the best performance was selected and its hyperparameters and grid scale were considered optimal. Finally, samples under the optimal grid scale were used to train the selected model, and test samples were used to verify its accuracy.

3.2.3.1. Automatic machine learning. Automatic Machine Learning (AutoML) is a powerful technology designed to automate the machine learning process, reducing the workload of researchers and data scientists while improving the efficiency and accuracy of model construction (Slimani et al., 2022). It streamlines critical steps such as feature engineering, model selection, and the model ensemble through automation, making the process of building and optimizing machine learning models more efficient and reliable (Salehin et al., 2024). In our study, we employed AutoML to compare the performance of 19 machine learning models at each spatial scale in simulating LST based on 50 built environmental features; therefore, we could evaluate and compare the performance of various models more rapidly, select the most suitable model for our research purposes, and lay the foundation for subsequent model interpretation and exploration of the impact of built environmental features on LST.

3.2.3.2. Bayesian optimization for hyperparameter tuning. Hyperparameters control the behavior of machine learning algorithms and have a significant impact on model accuracy (Wu et al., 2019). Therefore, it was necessary to adjust the hyperparameters of the machine learning model. Compared to traditional methods such as grid or random search, Bayesian optimization is more efficient because it can find the optimal configuration within a limited number of evaluations while considering uncertainty and prior information (Shang et al., 2020). We utilized Bayesian optimization to adjust the hyperparameters of the models that performed relatively well in AutoML and ultimately selected the best-performing model from all models at each spatial scale for subsequent analysis. During the optimization process, we set the number of iterations to 50 and scoring to r^2.

3.2.4. *Extreme gradient boosting*

As an advanced implementation of gradient boosting, extreme gradient boosting (XGBoost) sequentially constructs an ensemble of decision trees (Torlay et al., 2017). Each new tree attempts to correct the prediction errors of previous trees. For a dataset that includes n samples and m features, XGBoost formulates the predictions as

$$F = \{f_k(x) = W_{q(x}\}(q: R^m \rightarrow T,\ w \in R^m) \tag{9}$$

$$\widehat{p}_i = \varnothing(x) = \sum_{k=1}^{K} f_k(x_i),\ f_k \in F \tag{10}$$

where x_i represents the input feature vector in R^m, $\widehat{p}_i$ denotes the predicted value, represents the decision tree function, and K is the total number of trees. Each f_k consists of leaf weight w and tree structure function $q(x)$ (Niazkar et al., 2024). XGBoost differs from conventional boosting methods because of its training error and regularization term design (Mitchell & Frank, 2017). The former applies a loss function to measure the disparities between predicted and true values. The latter can be used for overfitting and can be written as follows:

$$\Omega(f_k) = \gamma T + 0.5\lambda \sum_{j=1}^{T} w_j^2 \tag{11}$$

$$Obj(\varnothing) = \sum_{i=1}^{n} L(p_i,\ \widehat{p}_i) + \sum_{k=1}^{K} \Omega f_k \tag{12}$$

where $\Omega(f_k)$ serves as regularization to control model complexity and prevent overfitting; γ is the leaf complexity; λ represents L2 wt regularization tern and w_j is the vector of the leaf score; L represents a differentiable loss function measuring prediction error; and p_i and $\widehat{p}_i$ represents the true and the predict value (Niazkar et al., 2024). XGBoost demonstrates superior computational speed compared to other ensemble classifiers such as AdaBoost. Its parallel-processing capability enables it to harness multicore computing resources, thereby making it efficient for training large-scale datasets (Asselman et al., 2023).

3.2.5. SHAP for important feature extraction

To explain the impact of different built environmental features on LST, we employed the SHAP method to interpret the optimal model. SHAP is an explanatory technique used to interpret model predictions. It is based on the concept of Shapley values from cooperative game theory, which measures the contribution of each feature to the prediction outcome. By calculating the Shapley values, SHAP provides a measure of the relative importance of each feature (Lu & Zhang, 2022) and illustrates how the features of each individual sample influence its prediction outcomes (Xue et al., 2024). Through SHAP, we not only obtained a global ranking of the importance of built environmental features but also understood the impact of each built environmental feature on the LST within each grid. Feature selection is necessary to avoid model redundancy (Lin et al., 2023). We added features, starting with two features in descending order of SHAP values, and trained the model. We stopped adding features when the accuracy of the model became stable and used the feature set at this moment as the final feature set (Xue et al., 2024).

3.2.6. Classification scheme of priority sites for LST mitigation

This study proposed a criterion for evaluating the urgency of building environmental improvements in grid cells. A warming feature is defined by a SHAP value greater than zero, indicating that it promotes increased LST. The number of warming features in each grid was counted as the count of warming features (CWF). By combining LST and CWF, the grid cells were divided into four classes:

1) Grids with above-average LST and CWF are "most emergency" areas. These areas have higher LST and require more effort from urban developers to improve the number of warming features.
2) Grids with below-average LST and CWF are "less emergency" areas, because these areas have fewer warming features, which may require fewer resources from urban developers to improve the UHI effects.
3) Grids with below-average LST but higher CWF are "remain concerned" areas. Although these areas do not exhibit higher LST, they have a significant number of warming features. This phenomenon may be attributed to the presence of a few crucial built environmental features that can significantly reduce LST. Therefore, urban developers need to invest efforts in preserving the significant cooling features.
4) Grids with below-average LST and CWF are "well-built" areas, with no significant UHI issues.

4. Results

4.1. Model performance

In this study, the Pycaret AutoML library was employed to fit and evaluate 19 models examining the building environment-LST relationship across six spatial scales. Table 3 summarizes the accuracy of several high-performance models following AutoML and Bayesian optimization. Results indicate that as the spatial scale increased, there was a notable improvement in the overall predictive performance of the models. Notably, the nonlinear models demonstrate superior performance at smaller spatial grids. However, with increasing spatial scale, the performance of certain linear models, such as linear regression, exceeds that of certain nonlinear models. The analysis revealed that after hyperparameter tuning, the XGBoost model yielded optimal results at a 210-m grid scale (R-squared (R^2) = 0.7916, Mean Squared Error (MSE) = 0.4378, Root Mean Squared Error (RMSE) = 0.6605, Mean Absolute Error (MAE) = 0.4995, Root Mean Squared Logarithmic Error (RMSLE) = 0.0234, and Mean Absolute Percentage Error (MAPE) = 1.932).

4.2. Feature importance evaluation

The findings presented in Section 4.1 indicate that the XGBoost algorithm exhibits optimal performance at a grid scale of 210 m. Prior to analyzing the impact of the built environment on LST, we conducted feature selection to optimize the model performance. Our initial dataset contained 50 features. After training the XGBoost model, we calculated the SHAP feature importance values for each feature. By incrementally adding features in descending order of importance and evaluating the model performance, we observed that the model accuracy-feature count relationship initially increased and subsequently plateaued (Fig. 3(a)). The optimal number of features was 25 as the accuracy curve began to stabilize at this threshold. This feature selection process enabled us to identify the most influential features while preserving the model efficiency.

Utilizing the optimized model with 25 features, Fig. 3 illustrates the relationship between the feature values and their corresponding SHAP values for all built environmental features across each grid, while ranking the importance of these features and their influence on LST in ascending order. Fig. 3(b–d) depict the relationship between the built environmental features and UHI within the land-use, GSV, and facility feature categories, respectively. The color gradient of each scatter point represents the feature value, whereas the horizontal coordinate indicates the corresponding SHAP value. Higher SHAP values signify stronger warming effects of the corresponding features on the LST. Results reveal that the proportion of woodland in the grid (woodland) emerges as the most important feature, demonstrating the most effective cooling impact on LST. Our analysis further indicates that this feature provides a more significant cooling effect than other vegetation types such as shrubs (shrubland). This finding aligns with the results of Lin et al. (Lin et al., 2023). Conversely, the proportions of warehouses and open storage (WH_and_OS), port facilities (Port_Facilities), and road and transport facilities (R_and_TF) in the grid were identified as the most significant contributors to increased LST. Additionally, road network density (road_len) and the proportion of trees in the horizontal view (mean_p_tree) emerged as the most important built environmental features influencing LST in the feature categories of facilities and GSV, respectively.

Fig. 3(e–j) demonstrate the correlation between feature values and

Table 3

Summary of performance of models in automated machine learning at different spatial scales.

Grid	Model	MAE	MSE	RMSE	R2	RMSLE	MAPE
60 m	Light Gradient Boosting Machine	0.6401	0.6536	0.8083	0.6089	0.0295	2.4236
	Gradient Boosting Regressor	0.6377	0.6507	0.8065	0.6107	0.0294	2.4153
	Extra Trees Regressor	0.6600	0.6945	0.8330	0.5848	0.0304	2.5003
	Random Forest Regressor	0.6658	0.7050	0.8393	0.5785	0.0306	2.5224
	eXtreme Gradient Boosting	0.6394	0.6567	0.8101	0.6070	0.0296	2.4221
90 m	Light Gradient Boosting Machine	0.6053	0.5836	0.7633	0.6693	0.0279	2.2989
	Extra Trees Regressor	0.6265	0.6214	0.7874	0.6481	0.0288	2.3803
	Gradient Boosting Regressor	0.6029	0.5801	0.7610	0.6712	0.0278	2.2907
	Random Forest Regression	0.6345	0.6374	0.7975	0.6389	0.0292	2.4107
	eXtreme Gradient Boosting	0.6009	0.5800	0.7611	0.6710	0.0279	2.2834
120 m	Ridge Regression	0.5863	0.5606	0.7486	0.7098	0.0274	0.0223
	Linear Regression	0.5871	0.5622	0.7497	0.7089	0.0274	0.0223
	Gradient Boosting Regressor	0.5670	0.5215	0.7220	0.7260	0.0265	2.1600
	Light Gradient Boosting Machine	0.5654	0.5154	0.7178	0.7293	0.0263	2.1544
	Extra Trees Regressor	0.5873	0.5586	0.7473	0.7066	0.0274	2.2373
150 m	Ridge Regression	0.5785	0.5390	0.7337	0.7282	0.0269	0.0221
	Linear Regression	0.5799	0.5394	0.7340	0.7280	0.0269	0.0221
	Light Gradient Boosting Machine	0.5515	0.4967	0.7038	0.7493	0.0259	2.106
	Extra Trees Regressor	0.5698	0.5309	0.7281	0.7317	0.0268	2.1774
	Gradient Boosting Regressor	0.5474	0.4921	0.7006	0.7516	0.0257	2.0905
180 m	Ridge Regression	0.5559	0.5015	0.7079	0.7544	0.0260	0.0212
	Linear Regression	0.5560	0.5070	0.7117	0.7514	0.0261	0.0212
	Light Gradient Boosting Machine	0.5518	0.4971	0.7039	0.7492	0.0259	2.1078
	Extra Trees Regressor	0.5571	0.5065	0.7107	0.7447	0.0261	2.1277
	eXtreme Gradient Boosting	0.5579	0.5113	0.7142	0.7416	0.0263	2.1315
210 m	Linear Regression	0.5198	0.4565	0.6750	0.7838	0.0249	0.0199
	Ridge Regression	0.5212	0.4598	0.6776	0.7824	0.0249	0.0200
	Light Gradient Boosting Machine	0.5129	0.4427	0.6644	0.7891	0.0244	1.9642
	Extra Trees Regressor	0.5362	0.4791	0.6917	0.7715	0.0254	2.0552
	eXtreme Gradient Boosting	**0.5148**	**0.4378**	**0.6605**	**0.7916**	**0.0243**	**1.9732**
240 m	Bayesian Ridge	0.4716	0.3535	0.5937	0.7332	0.0218	0.0180
	Huber Regressor	0.4864	0.3868	0.6188	0.7089	0.0227	0.0185
	Ridge Regression	0.4889	0.3788	0.6148	0.7144	0.0225	0.0186
	eXtreme Gradient Boosting	0.4872	0.4008	0.6323	0.6939	0.0231	1.8488
	Gradient Boosting Regresso	0.4867	0.4070	0.6371	0.6898	0.0233	1.8467

their corresponding SHAP values, providing insights into how building environment features influence LST. Examining woodlands (Fig. 3(e)) as a case study, there was a clear negative correlation between woodland values and SHAP values. When woodland coverage was below 0.1, the SHAP value remained positive, indicating that insufficient woodland coverage may contribute to temperature increases. The threshold of 0.1 marks a key turning point, where SHAP values transition from positive to negative, and cooling effects begin to manifest. This establishes a baseline for minimum woodland coverage in urban planning. Woodland areas demonstrate a strong cooling potential, with SHAP values ranging from +0.5 to −1.5. The cooling effect reaches its maximum when woodland coverage attains 0.8–1.0, with SHAP values reaching their minimum (−1.25 to −1.5).

Based on these findings, we propose that urban planning should ensure basic woodland coverage of no less than 10 %, with 30–40 % as the optimal target. Areas with less than 10 % woodland require urgent intervention. Areas with 10–30 % coverage should implement gradual increases. Areas with 30–80 % focus on maintenance and spatial configuration. Areas greater than 80 % necessitate strict protection. These recommendations, derived from the SHAP analysis, offer a more data-driven approach compared to traditional methods and provide enhanced guidance for urban cooling strategies.

Notably, features related to topography/surface area, such as DEM_std and the total volume of buildings in a grid (sum_volume), exhibit a positive correlation with LST. This finding is consistent with the research of (Yang et al., 2017), who observed the existence of relatively cooler built-up areas in high-density cities. We hypothesize that this phenomenon may be attributed to the fact that when an equal amount of solar radiation is incident upon a grid with greater topographic variations/surface area than on a flatter grid, the former absorbs less solar radiation per unit area, consequently resulting in a reduced increase in the LST.

4.3. Impact of built environmental feature classes on UHI

Fig. 4 illustrates the impact of different built environmental feature classes on LST within each grid, helping decision makers locate the major contributors within different grids that cause UHI. In general, most feature classes provide cooling effects at the edges of new towns and heating effects in their centers of new towns. When compared with the other two feature classes, the land-use/built environmental feature class had a greater influence on the change in LST. More specifically, it decreased LST in more than 50 % of the Tsuen Wan area and provided a significant cooling effect in regions south of Tai Po, southwest of Sha Tin, and northeast of Tsuen Wan-Kwai Chung, reducing LST by at least 1.5 °C. Furthermore, the land-use feature class had a more significant contribution to LST increases in the Hung Shui Kiu/Ha Tsuen, Yeun Long, Tsuen Wan-Tsing Yi, and Tsuen Wan-Kwai Chung areas. Among them, the land-use feature class had a serious impact on the central part of Hung Shui Kiu/Ha Tsuen, the northern part of Yeun Long, and the southern parts of Tsing Yi and Kwai Chung with an increase in LST of more than 1.5 °C. The impact of facility and GSV feature classes on LST is located in the range of [−1.5 °C, 1.5 °C], with the GSV feature class having a slightly more noticeable impact on LST compared to the facility feature class, particularly in regions such as Yuen Long north, Tuen Mun north, and Tai Po central, contributing more than ±0.5 °C. This suggests that land-use features have the most significant influence the UHI, whereas facility information has the least influence on UHI.

The importance of land-use feature classes can be understood from two perspectives. From the perspective of physical mechanisms, land use directly determines the physical properties of a surface. These properties include albedo, heat capacity, and evapotranspiration. Industrial land typically uses impervious materials such as asphalt and concrete. These materials exhibit high heat absorption and storage capacities. In contrast, green spaces and water bodies exhibit stronger cooling effects.

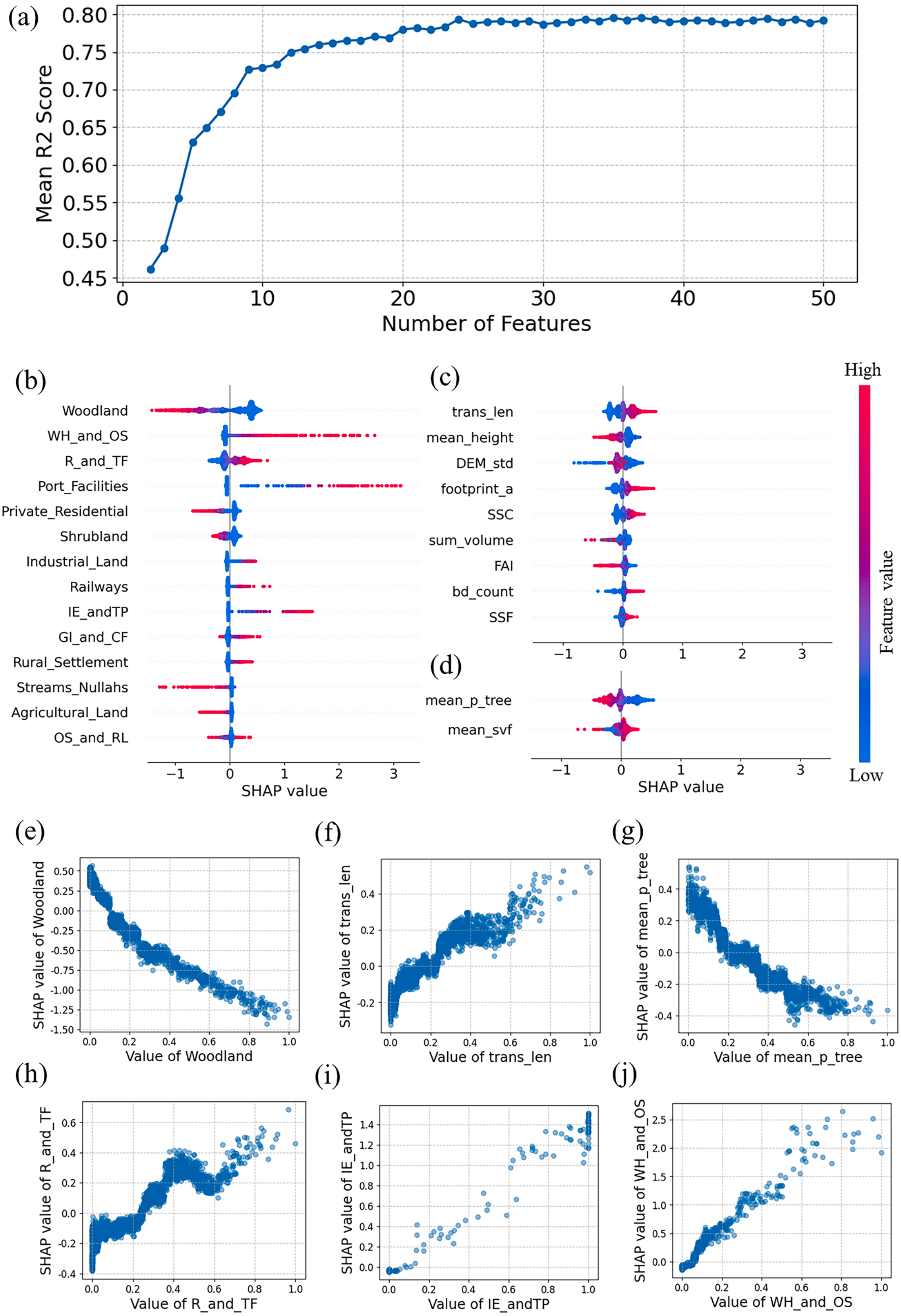

Fig. 3. Feature Importance Analysis: (a) Feature Quantity vs. Model Accuracy (R^2); (b-d) SHAP Value Performance by Feature Class (b: land-use feature class; c: facilities feature class; d: GSV feature class); (e-j) SHAP Dependence Plots for Individual Features (e: Woodland; f: trans_len; g: mean_p_tree; h: R_and_TF; i: IE_andTP; j: WH_and_OS).

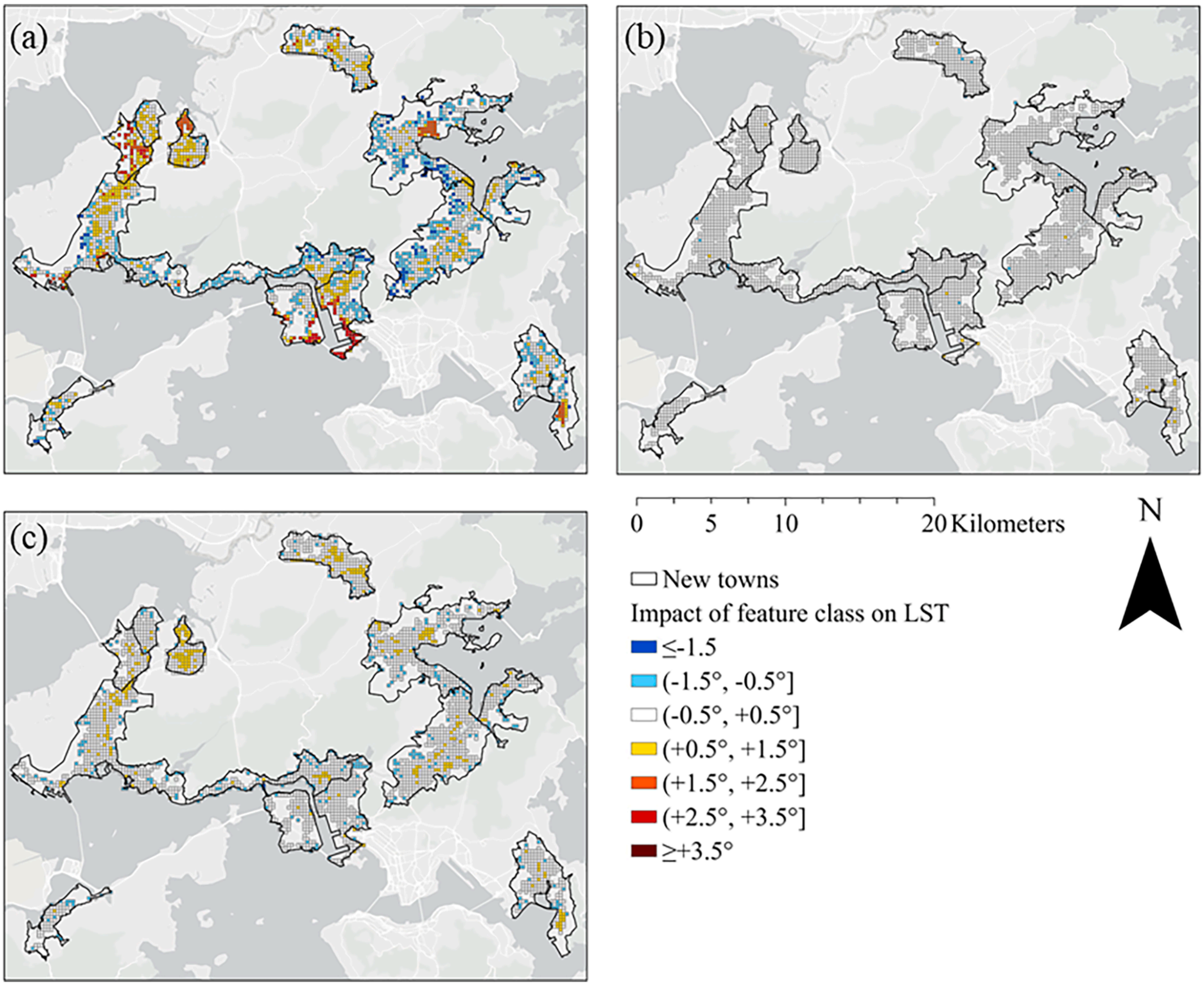

Fig. 4. Influence of (a) Land-use, (b) facilities, and (c) GSV feature class on LST.

This is due to their higher evapotranspiration rates and lower heat capacities. Second, from a methodological perspective, land use is a comprehensive indicator with a clear definition and low measurement error. This makes it exhibit stronger explanatory power in statistical analysis than other built environment characteristics.

This effect was particularly pronounced in areas with single, concentrated, and continuous land use, such as Tsuen Wan-Tsing Yi East and Tai Po Central. Areas, such as science parks and ports, are typically planned and built as unified functional units. This unified planning resulted in homogeneous facility construction and landscape design within these areas. Consequently, the facility and GSV features may exhibit similar patterns in these regions. The homogeneity of other built environmental characteristics highlights the importance of land-use features in these areas.

Fig. 5(a) illustrates the built environmental feature with the highest SHAP value within each 210-m grid, highlighting the largest UHI contributor in each area. This spatial distribution aids urban planners in identifying and targeting key features that contribute to local UHI. However, Fig. 5 does not depict the overall relationship between built environmental features and UHI; a single SHAP value only reflects the impact of a feature value on the sample prediction. As discussed in Section 4.2, woodlands and UHI are negatively correlated. However, in most grids, particularly new town centers, woodland was the largest UHI contributor owing to low woodland coverage. The model predicted a positive contribution of woodland to UHI, indicating that a lack of woodland increased UHI. Other significant contributors to UHI include WH_and_OS, Industrial Estates/Science and Technology Parks (IE_and TP), and port facilities. Port facilities and IE_and_TP, as major contributors to UHI, demonstrated notable spatial clustering. The former is predominantly concentrated in the Tsuen Wan-Tsing Yi and Tsuen Wan-Kwai Chung areas, whereas the latter is mainly distributed in northern Yuen Long, central Tai Po, and southern Tseung Kwan O. Fig. 5(b) depicts the most significant LST reduction features in grids where the surface temperature is below average. Similar to Fig. 5(a), woodland remained the most significant feature, indicating its crucial role in affecting LST. However, unlike the spatial clustering of the major UHI contributors shown in Fig. 5(a), the main cooling contributors in the low-LST grids are more dispersed. In the new towns of Hong Kong, GSV built environmental features significantly reduced surface temperatures. As the second most important factor in UHI mitigation, mean_p_tree shows a notable influence from the GSV feature class in nearly 30 % of the low LST grids in Fanling/Sheung Shui/Kwu Tung.

4.4. *Priority places of built-up area with the goal of reducing LST*

Fig. 6 illustrates the built-up areas with different priority levels **for** reducing surface temperature. The cumulative bar chart below each sub chart depicts the contribution of various built environmental features within the grid to UHI. The color of the column (red/blue) indicates whether the feature increases/decreases the LST, whereas the length of the column represents the magnitude of the LST increases/decreases.

Fig. 6(a) presents an example of a "most urgent" area, characterized by tall, dense buildings and large impervious surfaces. Private residential land use in this grid reduced UHI. We hypothesize that this was due

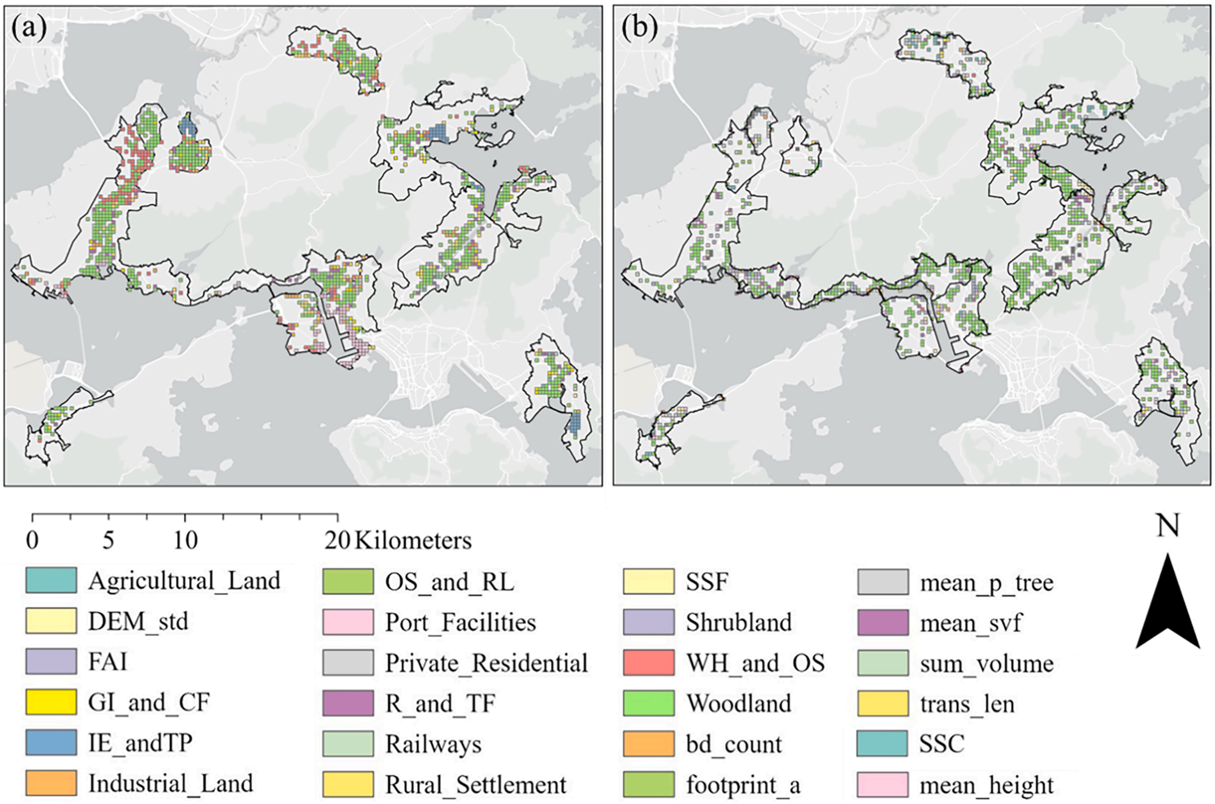

Fig. 5. Built environmental features in the new towns of Hong Kong with the (a) highest and (b) lowest SHAP values.

to better living environments in private residential areas (such as better greenery and less dense building arrangements). However, a high proportion of transportation land use and insufficient woodland areas constitute the main causes of UHI in this area.

Fig. 6(b) showcases an example of a "less urgent" grid. Compared to the "most urgent" grid, it exhibits lower building density, accompanied by low-rise buildings and limited vegetation (woodland/shrubland). This area has a limited number of heating factors. The excessive WH_and_OS areas and insufficient woodlands represent the main heating factors in this grid. Therefore, we suggest urban designers consider converting WH_and_OS areas into woodland to mitigate UHI.

Fig. 6(c) demonstrates a "remain concern" grid, characterized by varying topography, low building density, and sparse vegetation coverage (woodland/shrubland). Although this area has an above-average number of heating factors, the warming effects are not significant. Maintaining a certain woodland area can largely offset the UHI contribution from the heating factors.

Fig. 6(d) displays a "well-built area." This grid features varying topography and contains extensive woodlands and shrublands with limited transportation land use and low-rise buildings. The abundance of woodlands, trees in view, and minimal building footprint areas contribute to excellent cooling effects.

Fig. 7 illustrates the spatial distribution of the urgency levels for UHI mitigation. The "most emergency" areas and "well-built" areas dominate the majority of the region. The "most emergency" areas are primarily concentrated in certain regions in the eastern, central, and northern parts of the study area, whereas the distribution of "well-built" areas extends more widely beyond the central area of the new towns. There are significant differences in the proportions of grids with different urgency levels among the new towns. Yuen Long and Hun Shui Kui/Ha Tsuen are almost entirely covered by "most emergency" regions. Conversely, Sha Tin-Ma On Shan and Tung Chung had the highest proportions of "well-built" areas. The western and southern areas of Tsuen Wan-Keai Chung, eastern and central parts of Fanling/Sheung Shui/Kwu Tung, and Tuen Mun center exhibit distinct clustering of "most emergency" areas, requiring special attention during urban construction.

4.5. *Comparison of the importance of built environmental features in new towns*

Based on the temporal sequence of development, we analyzed the spatial heterogeneous characteristics between different new urban areas along two dimensions. First, we classified the new towns into three generations based on their initial construction time and examined the top 20 most influential features for each generation (Fig. 8). The analysis revealed that woodlands and mean_p_ trees were the most important features across all three generations. Port facilities significantly influenced LST in first-generation new towns but dropped to 17th place in importance for second- and third-generation new towns, reflecting both the geographical advantage of first-generation new towns (such as Tsuen Wan) with ports and the early planning strategy that prioritized areas with transportation advantages. Industrial land use ranked among the top ten most important features in the first two generations but fell to 18th place in the third generation, whereas the importance of private residential land use has continuously risen from seventh in the first generation to fourth in the third generation. This shift reflects the transformation from industrial zones to livable urban development as the city evolved as well as the increasing demand for quality living environments driven by economic development.

Furthermore, we investigated the impact of each feature on the LST for 13 individual new town regions, including Fanling/Sheung Shui/Kwo Tung, Hun Shui Kiu/Ha Tsuen, Tsuen Wan-Tsuen Wan, Yuen Long, Tsuen Wan-Tsing Yi, Tai Po, Sha Ting-Sha Ting, Tin Sgui Wai, Tsuen Wan-Kwai Chung, Tung Chung, Sha Tin-Ma On Shan, Tune Mun, and Tseung Kwan O individual new towns (see Appendix Fig. 1), revealing distinct patterns of spatial heterogeneity. The Tsuen Wan-Kwai Chung and Tsuen Wan-Tsing Yi areas showed more severe UHI, with port

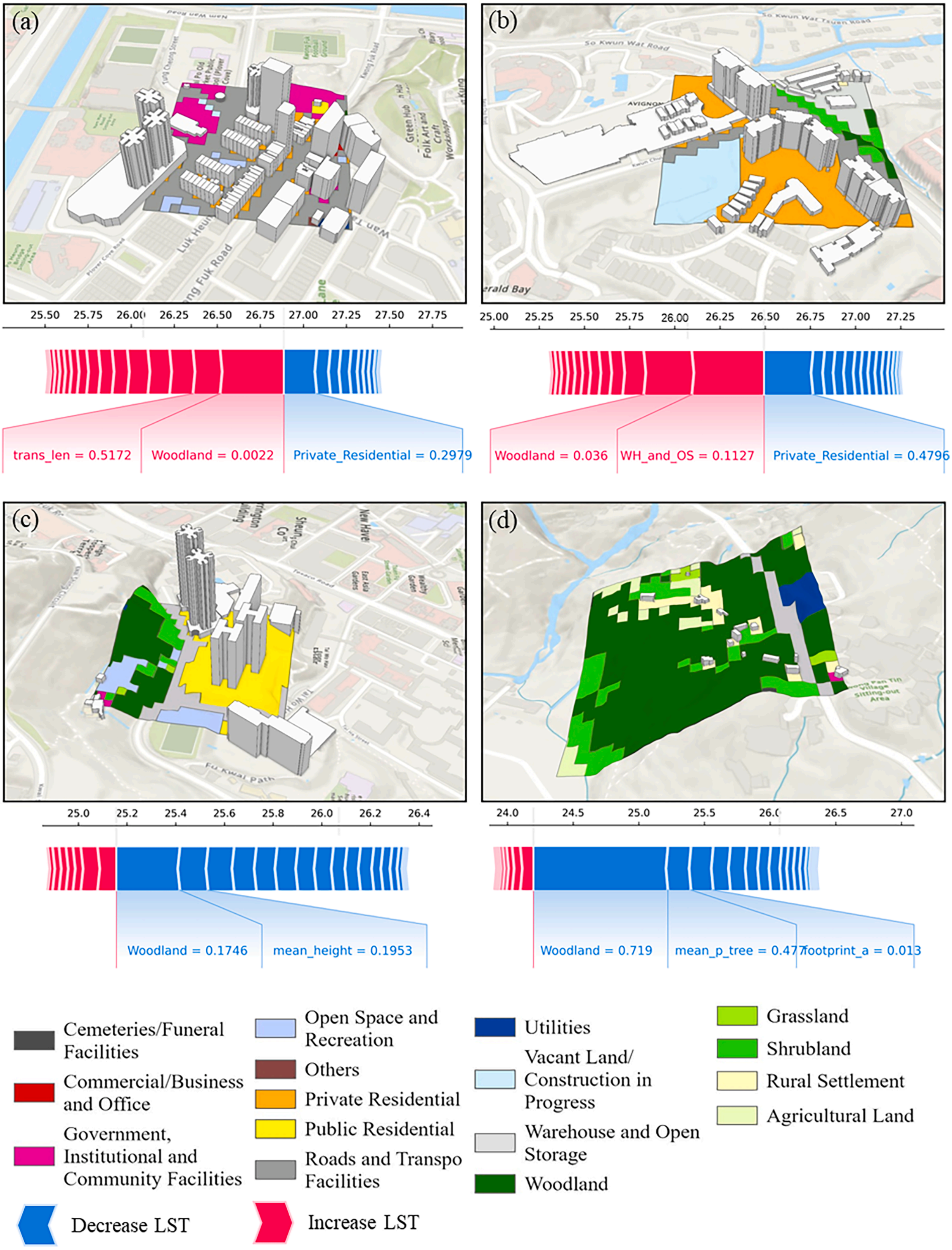

Fig. 6. Case studies of UHI mitigation priority areas: (a) “most emergency”, (b) “less emergency”, (c) “remain concern”, and (d) “well-built”, with statistics of built environment features’ impact on LST.

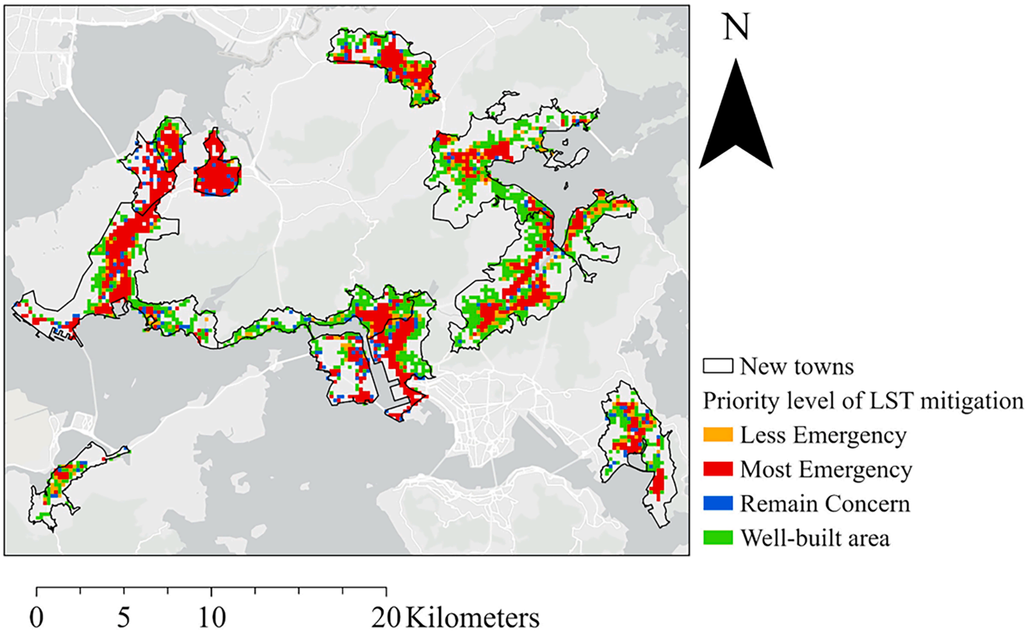

Fig. 7. Distribution of priority sites for LST mitigation.

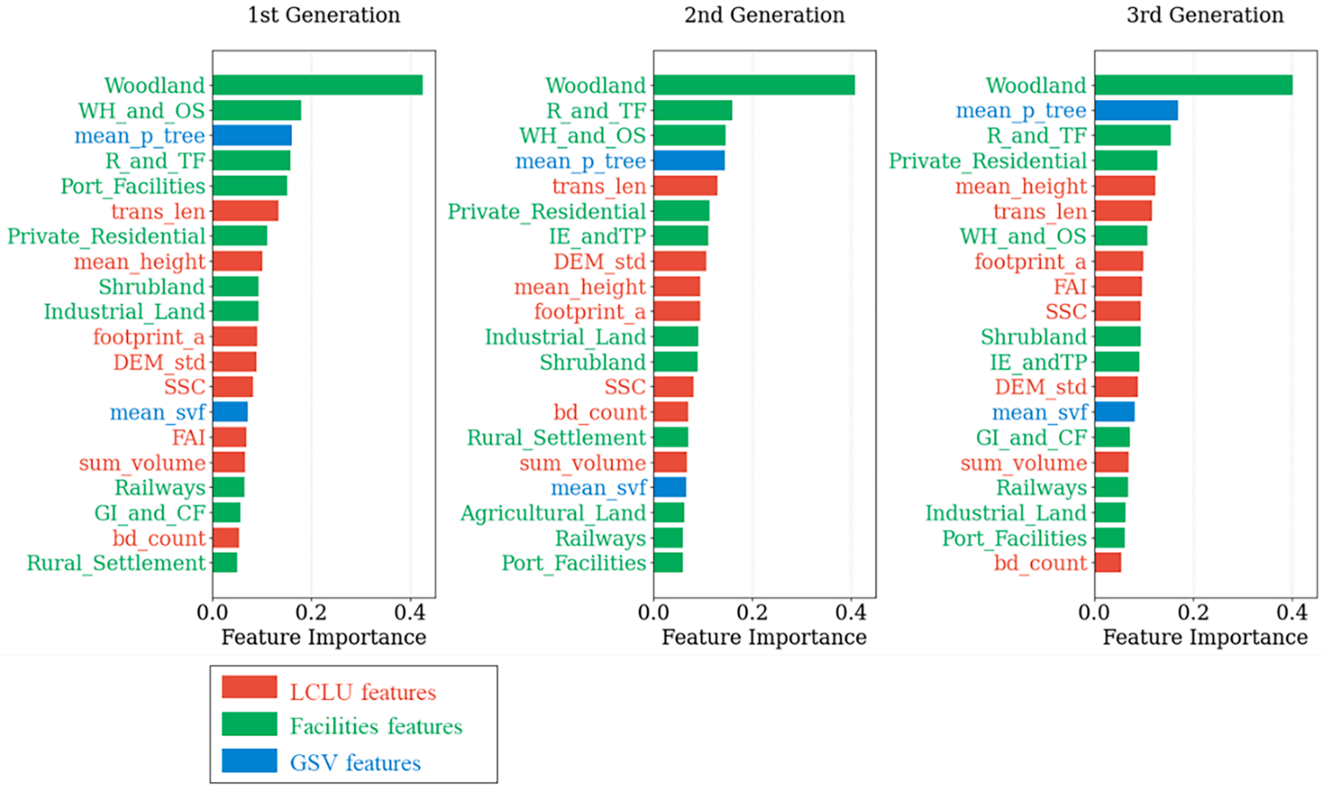

Fig. 8. Ranking of the top 20 most important built environmental features in three generations of new towns.

facilities and mean_p_tree being the main contributors to UHI in the former, whereas WH_and_OS and port facilities collectively contributed to UHI in the latter. In contrast, the UHI effect in Yuen Long was primarily caused by high proportions of industrial and public transport land use combined with low woodland coverage. Other new towns demonstrated lower UHI intensities, which was primarily attributed to higher woodland coverage, significant topographical variation, higher proportions of private residential areas, lower proportions of transport land use, and higher proportions of shrubland.

5. Discussion

5.1. Feature impact analysis of different plot types with a varying land-use mix

The SHAP decision plot visualizes the evolution of the predictions throughout the decision-making process (Fig. 9). The features are arranged along the y-axis based on their impact. The output of the model is represented on the x-axis. Starting from the base value, which is the sum of the SHAP values for all features, the plot traces the cumulative impact of the features from bottom to top until the final prediction is reached. This visualization reveals the magnitude of each feature throughout the estimation process.

First, the land-use entropy of each grid was calculated to quantify the degree of mixing. Using the elbow method in k-means clustering, we determined the optimal number of clusters to be four, thereby categorizing all grids into four plot types: low, medium-low, medium-high, and high. We randomly selected 150 samples from each category. Their SHAP decision plots are presented in Fig. 9.

Overall, as land-use mixing increased, the distribution of the corresponding LST became more dispersed, suggesting that complex land-use patterns had dual effects on the LST. Significantly, medium-high and high mix plot types demonstrated more favorable temperature regulation, with LST distributions primarily ranging between 26 and 32 °C, substantially lower than low and medium-low mix types (26–30.5 °C). We theorize that in highly mixed land-use patterns, different types can counterbalance one another, where warming effects from one type are often offset by cooling effects from others, resulting in more stable temperature regulation.

Woodland consistently appears as the most significant land-use type across all plot types. However, in high mix plot types, woodland configuration actually increased LST by over 0.5 °C in several grids, a phenomenon not evident in lower mix plot types. This anomaly likely originates from the spatial fragmentation of woodlands in highly mixed areas. When woodland is fragmented, it lacks the necessary continuity and scale effect to form effective cooling corridors, potentially creating localized "heat accumulation zones" around its periphery, thus reducing its cooling benefits.

In the low-mix grids, most areas demonstrated lower UHI values. However, several grids showed notably higher surface temperatures owing to high proportions of "warehouse and open storage" or "port facilities land.” We postulate that these grids are predominantly characterized by these land-use types. Their design lacks integration of cooling benefits, and the absence of diverse land-use compositions conducive to UHI reduction results in a significantly higher UHI effect. Such phenomena notably diminish as the complexity of land use increases. In the highest mix plot type, the importance of port facility land use decreases considerably, significantly increasing the UHI in only two grids.

5.2. Research innovations and contributions

This study advances our understanding of UHI through three main innovations. We developed a new framework based on SHAP spatial distribution analysis, expanded the scope of built environmental variables, and revealed the regional patterns of UHI formation. These innovations address important gaps in current research and provide practical insights for urban planning and UHI mitigation.

We proposed a research framework that integrates machine learning with SHAP spatial analysis for UHI studies. This framework utilizes the spatial distributions of SHAP values to explain how the built environment affects UHI patterns across space. Although many machine

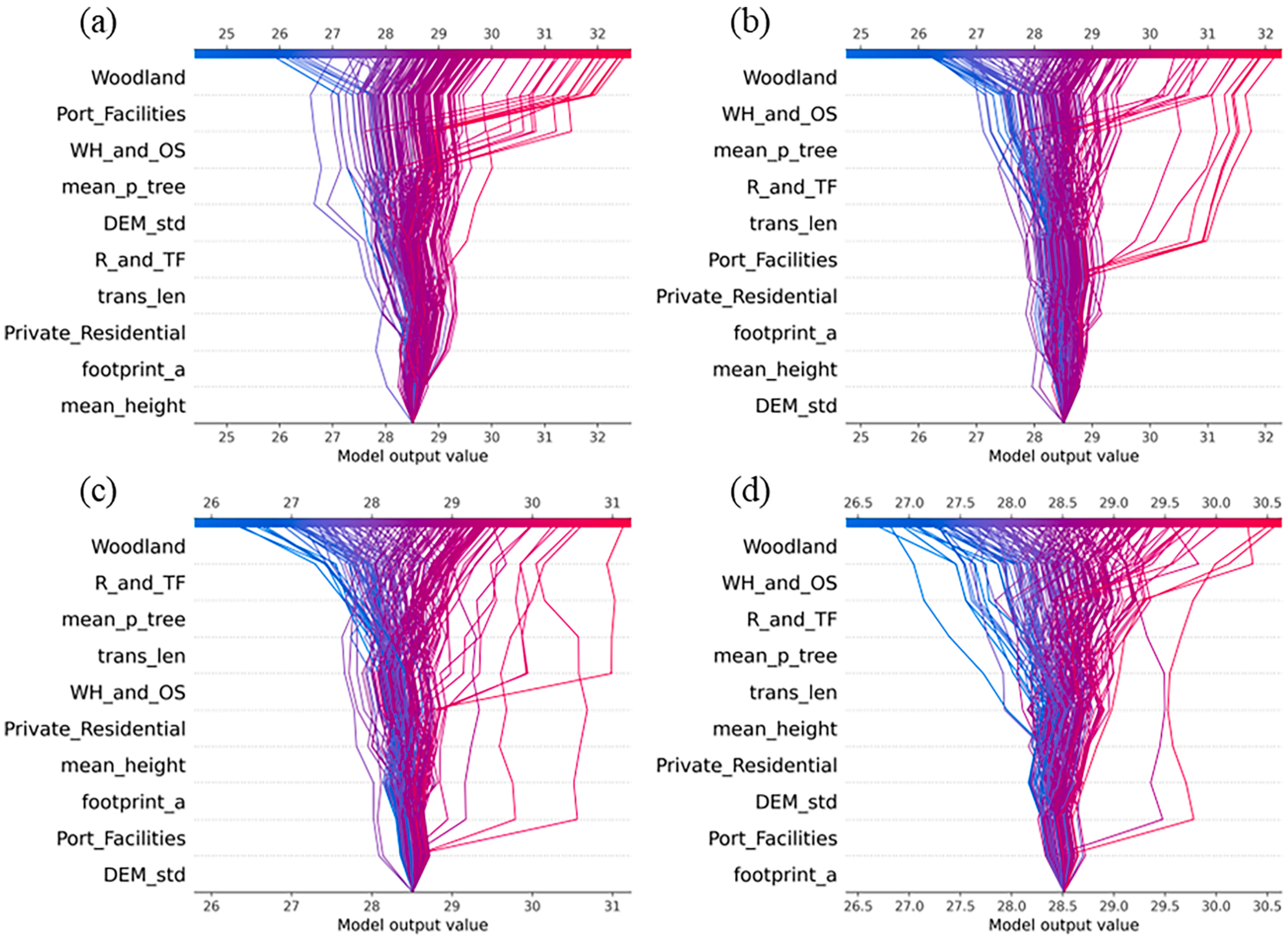

Fig. 9. Influence of built environmental features on plot types with (a) low; (b) medium low; (c) medium high; and (d) high land mix.

learning studies have examined the overall importance of built environmental factors on surface temperature, they have often neglected the spatial variations in these effects. Studies focusing on spatial variations have mainly employed linear models such as GWR, which fail to adequately capture the complex relationships between built environmental features and temperature. By analyzing the SHAP value distributions, we can identify both the nonlinear contributions of different factors to the temperature and how these contributions vary across space, offering new insights into UHI formation.

We implemented a more comprehensive approach to measure the built environment. Our study considered 50 built environmental features and selected 25 features encompassing land use, urban facilities, and street-level information. Previous studies have typically limited their analysis to 5–15 variables (Ghazaleh Tanoori & Atoosa, 2024; Liu et al., 2024; Bansal & Quan, 2023; Han et al., 2023; Erdem Okumus & Terzi, 2021; Ming et al., 2024). By including more variables, we conducted a more thorough assessment of the built environment and uncovered overlooked but important factors such as DEM_std. Our multidimensional analysis also facilitated a comparison of impacts across different planning levels. The findings indicate that land-use features exerted stronger effects than GSV and facility features. This understanding of the impact levels can assist relevant departments in making better decisions regarding resource allocation and coordination.

Our findings support more localized policy recommendations. Previous research often focused on the overall importance of variables (Wu et al., 2019; Yuan et al., 2024; Zhu et al., 2024), leading to broad policy suggestions like "properly arrange urban green spaces" (Yuan et al., 2024) or "minimize disruption to large urban green spaces" (Lin, Zhao et al., 2024). Through spatial analysis of SHAP values, we identified spatial patterns that previous studies have rarely addressed. For example, port facilities exert the strongest impact on coastal Kwai Chung, whereas industrial land use emerges as the main UHI contributor in northern Yuen Long. These spatial insights enable us to formulate more targeted local policy recommendations, demonstrating that UHI management requires different approaches for different areas rather than a one-size-fits-all solution.

5.3. Policy recommendations for addressing UHI in Hong Kong

Based on our proposed SHAP value spatial distribution analysis, we developed a three-level application strategy for refined UHI management: First, utilizing the SHAP priority distribution map of UHI intensity (Fig. 8), we identified priority areas requiring thermal environment improvement. The analysis reveals that the Hung Shui Kiu/Ha Tsuen and Yuen Long areas are almost entirely covered by "most emergency" grids, establishing them as top priority locations for thermal environmental renovation. Specific parts of Tsuen Wan (coastal areas of Tsing Yi and northern and coastal areas of Kwai Chung) also exhibit relatively large clusters of "most emergency" grids, positioning them as secondary priority areas. This SHAP value-based spatial priority assessment provides a robust scientific foundation for urban renovation planning.

Second, based on the spatial distribution patterns of the main UHI contributors (Fig. 5), we can assist policymakers in identifying key urban design issues across different areas. The findings indicate significant variations in the dominant factors within priority renovation areas: high temperatures in Hung Shui Kiu/Ha Tsuen are strongly associated with concentrated warehouse land use and open storage yards; Yuen Long demonstrates clear spatial differentiation, with northern areas mainly affected by industrial land use and central/southern areas by insufficient woodland. The coastal areas of both Tsing Yi and Kwai Chung were primarily affected by port facilities, which could potentially be simultaneously renovated.

Finally, by combining the quantitative relationships between the feature values and SHAP values illustrated in Fig. 3(e–j), we propose the following specific improvement strategies: (1) For Hung Shui Kiu/Ha Tsuen: Maintain WH_and_OS values below 0.4, to potentially reduce its contribution to LST by approximately 1° In instances where this value must exceed 0.4, implement increased woodland and vertical greenery on warehouse walls alongside street trees to maintain woodland/mean_p_tree values above 0.3/0.5, potentially providing a 0.2–0.5° cooling effect. (2) For Yuen Long: restrict IE_and_TP coverage to below 0.5 in northern areas to limit its LST contribution to less than 0.6°; establish woodland baseline values that exceed 0.1 in central/southern areas.

This systematic approach of "identifying priority renovation areas-analyzing dominant UHI factors-providing quantitative guidelines" enables decision-makers to develop targeted improvement strategies for specific issues in different areas. Government departments can better allocate resources and develop locally appropriate renovation plans. This hierarchical governance approach, from macro to micro and from the overall framework to specific measures, may help improve both precision in UHI management and the efficient use of renovation resources.

Our method can serve as a valuable decision support tool for future urban planning. Planning departments can use the model to predict the potential temperature impacts of different built environmental factors during new district planning and optimize thermal environmental effects by adjusting the spatial configuration and proportions of various elements. For example, our research indicates that high- and medium-high mixed land-use patterns may have better temperature regulation effects. However, in highly mixed land-use patterns, improper woodland configurations could potentially increase the warming effects. Therefore, we recommend prioritizing medium-high land-use mixing in urban design while ensuring sufficient, continuous woodland in highly mixed areas. Furthermore, given that trees and vegetation show significant potential for mitigating UHI effects, areas with limited horizontal green space can incorporate vertical vegetation (such as green walls) to supplement green space and mitigate local UHI effects.

5.4. Limitations and future work

Our study had several limitations. We analyzed the UHI patterns only under clear summer conditions. Although this represents the period when heat-related issues are most severe, it does not capture how the UHI varies with season and weather conditions. Although we compared the UHI-built environmental relationships between new towns in different development periods, we did not fully explore how the urban development process influenced these relationships over time. Additionally, our calculations of SSF and SSC only considered direct solar radiation and neglected building reflections and shadow overlaps. This may have led to imprecise urban shadow simulation, potentially introducing errors in our UHI modeling and assessment of the importance of shadow-related built environmental features.

Based on these limitations, we can identify improvements for future work. First, it only utilized data from a single period. Future studies could incorporate data spanning longer time frames to analyze variations across different seasons and years, providing a more comprehensive understanding of the dynamic changes in the urban heat island effect. Second, this study only examined the relationship between the built environment and UHI effect, omitting natural environmental and socioeconomic factors. This limitation suggests that the existing LST fitting model still has potential for precision improvement. Future research should continue to explore the impact of other environmental factors on the LST and incorporate more data sources to improve the prediction accuracy and applicability of the model, thereby further supporting the sustainable development of new towns.

6. Conclusion

This study integrated multi-source data, including remote sensing, street views, land use, road networks, and building footprints, to explore the impacts of built environmental features on UHI in the new towns in

Hong Kong. Using automated machine learning methods, we conducted quantitative analyses at different spatial scales and employed SHAP to interpret the model, further revealing the dominant roles of various features in different regions. The results indicate that XGBoost performs best at the 210-m grid scale. We also found significant relationships between the built environmental characteristics and LST, with the land-use feature class having the most significant impact. Additionally, based on LST and CWF, we identified that the areas which most in need of optimizing the built environment to mitigate UHI were Yuen Long and Hun Shui Kui/Ha Tsuen. This study provides urban developers with specific recommendations based on spatial heterogeneity, aiding in the optimization of urban layouts and the selection of reasonable urban designs in new town development to effectively mitigate the UHI effect. However, this study has several limitations. First, it only utilized data from a single period. Future studies could consider using data spanning longer time frames to analyze variations across different seasons and years, providing a more comprehensive understanding of the dynamic changes in the urban heat island effect. Second, this study only discussed the relationship between the built environment and the UHI effect, neglecting natural environmental and socioeconomic factors. This oversight suggests that the existing LST fitting model still has potential for precision improvement. Future research should continue to explore the impact of other environmental factors on LST and incorporate more data sources to improve the prediction accuracy and applicability of the model, thereby further supporting the sustainable development of new towns.

Declaration of generative AI and AI-assisted technologies in the writing process

During the preparation of this work the author(s) used ChatGPT in order to improve the readability and language of the manuscript. After using this tool/service, the author(s) reviewed and edited the content as needed and take(s) full responsibility for the content of the published article.

CRediT authorship contribution statement

Yiyan Li: Writing – review & editing, Writing – original draft, Visualization, Software, Methodology, Data curation. **Hongsheng Zhang:** Writing – review & editing, Funding acquisition. **Yinyi Lin:** Writing – review & editing. **Jing Ling:** Writing – review & editing, Conceptualization. **Huiyuan Xue:** Methodology. **Peizhuo Guo:** Methodology.

Declaration of competing interest

The authors declare that they have no known competing financial interests or personal relationships that could have appeared to influence the work reported in this paper.

Acknowledgements

This study was jointly supported by the National Natural Science Foundation of China (Grant No. W2412136); the Research Grants Council (RGC) of Hong Kong, China (HKU27602020, HKU17613022); the Croucher Foundation (CAS22902/CAS22HU01), Hong Kong, China; and the Seed Funding for Strategic Interdisciplinary Research Scheme of The University of Hong Kong, Hong Kong, China.

Appendix

Appendix Fig. 1

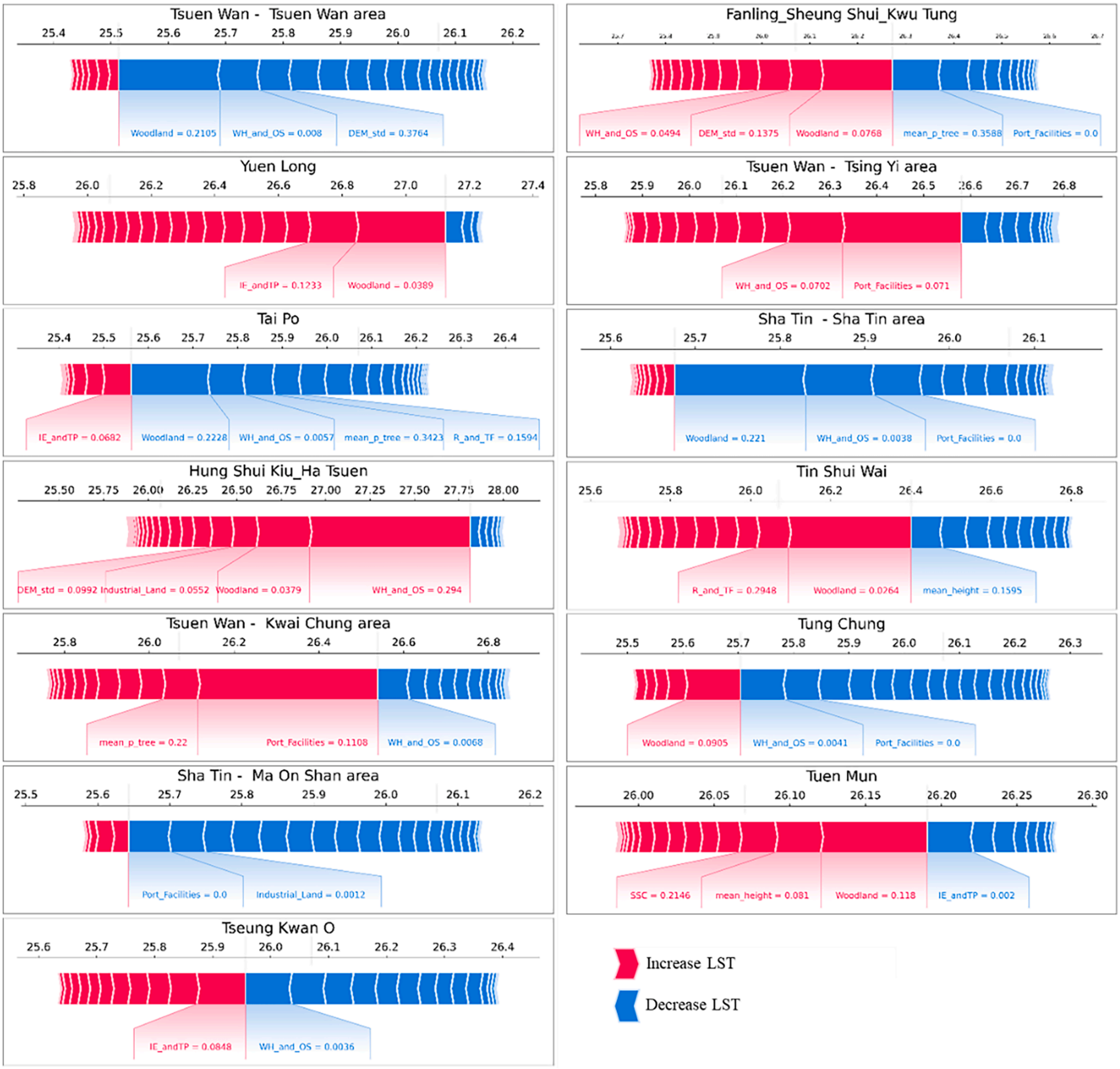

Appendix Fig. 1. Key warming/cooling built environmental features of new towns.

Data availability

Data will be made available on request.

References

Acosta, M. P., et al. (2023). A comprehensive generalizability assessment of data-driven Urban Heat Island (UHI) models. *Sustainable Cities and Society, 96*, Article 104701.

Aleksandrowicz, O., Saroglou, T., & Pearlmutter, D. (2023). Evaluation of summer mean radiant temperature simulation in ENVI-met in a hot Mediterranean climate. *Building and Environment, 245*, Article 110881.

Asselman, A., Khaldi, M., & Aammou, S. (2023). Enhancing the prediction of student performance based on the machine learning XGBoost algorithm. *Interactive Learning Environments, 31*(6), 3360–3379.

Aydin, E. E., et al. (2024). Climate-responsive urban planning through generative models: Sensitivity analysis of urban planning and design parameters for urban heat island in Singapore's residential settlements. *Sustainable Cities and Society, 114*, Article 105779.

Bagyaraj, M., et al. (2023). A study of urban heat island effects using remote sensing and GIS techniques in Kancheepuram, Tamil Nadu, India. *Urban Climate, 51*, Article 101597.

Balany, F., Ng, A. W., Muttil, N., Muthukumaran, S., & Wong, M. S. (2020). Green Infrastructure as an Urban Heat Island Mitigation Strategy—A Review. *Water*.

Banerjee, S., et al. (2024). Assessing impact of urban densification on outdoor microclimate and thermal comfort using ENVI-met simulations for Combined Spatial-Climatic Design (CSCD) approach. *Sustainable Cities and Society, 105*, Article 105302.

Bansal, P., & Quan, S. J. (2023). Examining temporally varying nonlinear effects of urban form on urban heat island using explainable machine learning: A case of Seoul. *Building and Environment*, 247.

Chen, Y., et al. (2025). The impacts and thresholds detection of 2D/3D urban morphology on the heat island effects at the functional zone in megacity during heatwave event. *Sustainable Cities and Society, 118*, Article 106002.

Chiang, Y.-C., et al. (2023). Quantification through deep learning of sky view factor and greenery on urban streets during hot and cool seasons. *Landscape and Urban Planning, 232*, Article 104679.

Civil Engineering and Development Department, HKSAR Government. (2016). *Hong Kong: The facts—New towns, new development areas and urban developments* [Brochure]. GovHK.. https://www.gov.hk/en/about/abouthk/factsheets/docs/towns&urban_developments.pdf.

Cornu, T., Marchal, B., & Renmans, D. (2024). How do urban green spaces influence heat-related mortality in elderly? A realist synthesis. *BMC public health, 24*(1), 457.

Cui, D., et al. (2024). Effects of vertical greening on the thermal environment and energy consumption in different street canyons. *Sustainable Cities and Society, 117*, Article 105979.

Darbani, E. S., et al. (2023). Urban design strategies for summer and winter outdoor thermal comfort in arid regions: The case of historical, contemporary and modern urban areas in Mashhad. *Iran. Sustainable Cities and Society, 89*, Article 104339.

do Nascimento, A. C. L., et al. (2022). Comparison between air temperature and land surface temperature for the city of São Paulo. *Brazil. Atmosphere, 13*(3), 491.

Erdem Okumus, D., & Terzi, F. (2021). Evaluating the role of urban fabric on surface urban heat island: The case of Istanbul. *Sustainable Cities and Society*, 73.

Gao, Y., Zhao, J., & Han, L. (2022). Exploring the spatial heterogeneity of urban heat island effect and its relationship to block morphology with the geographically weighted regression model. *Sustainable Cities and Society, 76*, Article 103431.

Ghazaleh Tanoori, S., A., & Atoosa, Modiri (2024). Machine Learning for Urban Heat Island (UHI) Analysis: Predicting Land Surface Temperature (LST) in Urban Environments. *Urban Climate*, 55.

Giridharan, R., Lau, S. S. Y., Ganesan, S., & Givoni, B. (2007). Urban design factors influencing heat island intensity in high-rise high-density environments of Hong Kong. *Building and Environment, 42*(10), 16.

Guattari, C., Evangelisti, L., & Balaras, C. A. (2018). On the assessment of urban heat island phenomenon and its effects on building energy performance: A case study of Rome (Italy). *Energy and Buildings, 158*, 605–615.

Han, D., An, H., Cai, H., Wang, F., Xu, X., Qiao, Z., Jia, K., Sun, Z., & An, Y. (2023). How do 2D/3D urban landscapes impact diurnal land surface temperature: Insights from block scale and machine learning algorithms. *Sustainable Cities and Society*, 99.

Heaviside, C., Macintyre, H., & Vardoulakis, S. (2017). The urban heat island: implications for health in a changing environment. *Current environmental health reports, 4*, 296–305.

Hu, Y., Dai, Z., & Guldmann, J.-M. (2020). Modeling the impact of 2D/3D urban indicators on the urban heat island over different seasons: A boosted regression tree approach. *Journal of environmental management, 266*, Article 110424.

Huang, Q., et al. (2019). Quantifying the seasonal contribution of coupling urban land use types on Urban Heat Island using Land Contribution Index: A case study in Wuhan. *China. Sustainable Cities and Society, 44*, 666–675.

Islam, S., et al. (2024). Urban heat island effect in India: a review of current status, impact and mitigation strategies. *Discover Cities, 1*(1), 1–28.

Jiang, Z., et al. (2024). The regional differentiation on the spatial distribution and influencing factors of potential landslides across the entire Loess Plateau, China based on InSAR and sub-region XGBoost-SHAP model. *IEEE Journal of Selected Topics in Applied Earth Observations and Remote Sensing*.

Kim, Y., & Kim, Y. (2022). Explainable heat-related mortality with random forest and SHapley Additive exPlanations (SHAP) models. *Sustainable Cities and Society, 79*, Article 103677.

Li, X., et al. (2018). Creating a seamless 1 km resolution daily land surface temperature dataset for urban and surrounding areas in the conterminous United States. *Remote Sensing of Environment, 206*, 84–97.

Li, Z., et al. (2023). 3D urban landscape optimization: From the perspective of heat flux-microclimate relations. *Sustainable Cities and Society, 97*, Article 104759.

Lin, J., et al. (2023). Measuring the relationship between morphological spatial pattern of green space and urban heat island using machine learning methods. *Building and Environment, 228*, Article 109910.

Lin, J., Wei, K., & Guan, Z. (2024). Exploring the connection between morphological characteristic of built-up areas and surface heat islands based on MSPA. *Urban Climate, 53*, Article 101764.

Lin, J., Zhang, H., Chen, M., & Wang, Q. (2023). Socioeconomic disparities in cooling and warming efficiencies of urban vegetation and impervious surfaces. *Sustainable Cities and Society*, 92.

Lin, L., Zhao, Y., Zhao, J., & Wang, D. (2024). Comprehensively assessing seasonal variations in the impact of urban greenspace morphology on urban heat island effects: A multidimensional analysis. *Sustainable Cities and Society*, 118.

Ling, Jing, K.H.A.Y, Wei, Shan, Sit, Ka Ying, Sun, Liqun, Meng, Qingyan, Cong, Na, & Lin, Jian (2024). Hongsheng Zhang Multiscale rooftop greening and its socioeconomic implications in Hong Kong. *Building and Environment*, 259.

Litardo, J., et al. (2020). Urban Heat Island intensity and buildings' energy needs in Duran, Ecuador: Simulation studies and proposal of mitigation strategies. *Sustainable cities and society, 62*, Article 102387.

Liu, R., Zhang, H., Yip, K. H. A., Ling, J., Lin, Y., & Huang, H. (2023). Automatic building height estimation with shadow correction over heterogeneous compact cities using stereo Gaofen-7 data at sub-meter resolution. *Journal of Building Engineering*, 69.

Liu, Y., An, Z., & Ming, Y. (2024). Simulating influences of land use/land cover composition and configuration on urban heat island using machine learning. *Sustainable Cities and Society*.

Lu, J., & Zhang, Y. (2022). Unified deep learning model for multitask reaction predictions with explanation. *Journal of chemical information and modeling, 62*(6), 1376–1387.

Lu, Y. (2018). The association of urban greenness and walking behavior: Using google street view and deep learning techniques to estimate residents' exposure to urban greenness. *International journal of environmental research and public health, 15*(8), 1576.

Ming, Y., Liu, Y., Li, Y., & Song, Y. (2024). Unraveling nonlinear and spatial non-stationary effects of urban form on surface urban heat islands using explainable spatial machine learning. *Computers, Environment and Urban Systems*, 114.

Mitchell, R., & Frank, E. (2017). Accelerating the XGBoost algorithm using GPU computing. *PeerJ Computer Science, 3*, e127.

Niazkar, M., et al. (2024). Applications of XGBoost in water resources engineering: A systematic literature review (Dec 2018–May 2023). *Environmental Modelling & Software*, Article 105971.

Park, Y., Guldmann, J.-M., & Liu, D. (2021). Impacts of tree and building shades on the urban heat island: Combining remote sensing, 3D digital city and spatial regression approaches. *Computers, Environment and Urban Systems, 88*, Article 101655.

Park, Yujin, Z, Q., Guldmann, Jean-Michel, & Wentz, Elizabeth A (2023). Quantifying the cumulative cooling effects of 3D building and tree shade with high resolution thermal imagery in a hot arid urban climate. *Landscape and Urban Planning*, 240.

Planning Department, The Government of the Hong Kong Special Administrative Region. (2023). *Land Utilization in Hong Kong: 2023 data*. https://www.pland.gov.hk/pland_en/info_serv/digital_planning_data/matrix/LUHK_2023.html.

United Nations, Department of Economic and Social Affairs, Population Division (UNDESA). (2018). World Urbanization Prospects: The 2018 Revision, Online Edition.

Qiang Chen, M. D., Liu, Rui, Cheng, Qianhao, & Li, Kangning (2023). Evaluating the impact of sky view factor and building shadow ratio on air temperature in different residential and commercial building scenarios: A case study of Beijing, China. *Urban Climate*, 49.

Salehin, I., et al. (2024). AutoML: A systematic review on automated machine learning with neural architecture search. *Journal of Information and Intelligence, 2*(1), 52–81.

Shang, Q., Feng, L., & Gao, S. (2020). A hybrid method for traffic incident detection using random forest-recursive feature elimination and long short-term memory network with Bayesian optimization algorithm. *IEEE Access, 9*, 1219–1232.

Shi, Y., Xiang, Y., & Zhang, Y. (2019). Urban design factors influencing surface urban heat island in the high-density city of Guangzhou based on the local climate zone. *Sensors, 19*(16), 3459.

Singh, M., Sharston, R., & Murtha, T. (2024). Critical Evaluation of the Spatiotemporal Behavior of UHI, through Correlation Analyses based on Multi-City Heterogeneous Dataset. *Sustainable Cities and Society*, Article 105576.

Sinsel, T., et al. (2022). Implementation and evaluation of mean radiant temperature schemes in the microclimate model ENVI-met. *Urban Climate, 45*, Article 101279.

Slimani, I., et al. (2022). Automated machine learning: the new data science challenge. *Int. J. Electr. Comput. Eng., 12*(4), 4243–4252.

Torlay, L., et al. (2017). Machine learning–XGBoost analysis of language networks to classify patients with epilepsy. *Brain informatics, 4*, 159–169.

Wang, Q., et al. (2023). Exploring the impact of urban features on the spatial variation of land surface temperature within the diurnal cycle. *Sustainable Cities and Society, 91*, Article 104432.

Wang, Z., et al. (2021). Environmental and anthropogenic drivers of surface urban heat island intensity: A case-study in the Yangtze River Delta. *China. Ecological Indicators, 128*, Article 107845.

Wang, Z., et al. (2024). Revealing the impact of Urban spatial morphology on land surface temperature in plain and plateau cities using explainable machine learning. *Sustainable Cities and Society*, Article 106046.

Wei, X., et al. (2023). Integrating planar and vertical environmental features for modelling land surface temperature based on street view images and land cover data. *Building and Environment, 235*, Article 110231.

Werner, M., Dax, G., & Laass, M. (2021). *Computational challenges for artificial intelligence and machine learning in environmental research*.

Wu, J., et al. (2019). Hyperparameter optimization for machine learning models based on Bayesian optimization. *Journal of Electronic Science and Technology, 17*(1), 26–40.

Xue, H., et al. (2024). Integrating visual factors in crash rate analysis at Intersections: An AutoML and SHAP approach towards cycling safety. *Accident Analysis & Prevention, 200*, Article 107544.

Yang, J., et al. (2019). Spatial differentiation of urban wind and thermal environment in different grid sizes. *Urban Climate, 28*, Article 100458.

Yang, X., et al. (2017). The urban cool island phenomenon in a high-rise high-density city and its mechanisms. *International Journal of Climatology, 37*(2), 890–904.

Yang, Z., et al. (2022). The impact of topographic relief on population and economy in the southern Anhui mountainous area. *China. Sustainability, 14*(21), Article 14332.

Yang, Q., et al. (2023). Influence of urban extent discrepancy on the estimation of surface urban heat island intensity: A global-scale assessment in 892 cities. *Journal of Cleaner Production, 426*, Article 139032.

Yin, C., et al. (2018). Effects of urban form on the urban heat island effect based on spatial regression model. *Science of the Total Environment, 634*, 696–704.

Yuan, B., Zhou, L., Hu, F., & Wei, C. (2024). Effects of 2D/3D urban morphology on land surface temperature: Contribution, response, and interaction. *Urban Climate*, 53.

Zhang, N., et al. (2022). Block-based variations in the impact of characteristics of urban functional zones on the urban heat island effect: A case study of Beijing. *Sustainable Cities and Society, 76*, Article 103529.

Zhang, T., et al. (2022). A global dataset of daily near-surface air temperature at 1-km resolution (2003–2020). *Earth System Science Data Discussions*, 1–18.

Zhang, H., et al. (2022). Resnest: Split-attention networks. In *Proceedings of the IEEE/CVF conference on computer vision and pattern recognition*.

Zhang, Y., et al. (2024). Optimizing Urban Green Space Configurations for Enhanced Heat Island Mitigation: A Geographically Weighted Machine Learning Approach. *Sustainable Cities and Society*, Article 106087.

Zhang, Z., Zhao, L., & Zhang, M. (2024). Exploring Non-linear Urban Vibrancy Dynamics in Emerging New Towns: A Case Study of the Wuhan Metropolitan Area. *Sustainable Cities and Society*, Article 105580.

Zhou, B., Zhao, H., Puig, X., Fidler, S., Barriuso, A., & Torralba.Scene, A. (2017). *Parsing through ADE20K Dataset. Computer Vision and Pattern Recognition (CVPR)*.

Zhou, H., et al. (2022). Outdoor thermal environment on road and its influencing factors in hot, humid weather: A case study in Xuzhou City. *China. Building and Environment, 207*, Article 108460.

Zhou, M., Wang, R., & Guo, Y. (2024). How urban characteristics impact surface urban heat island in subtropical high-density cities based on LCZs: A case study of Macau. *Sustainable Cities and Society*, Article 105587.

Zhu, S., Yan, Y., Zhao, B., & Wang, H. (2024). Assessing the impact of adjacent urban morphology on street temperature: a multisource analysis using random forest and SHAP. *Building and Environment*.